

Numerical Modeling of Concrete Using a Partially Associative Plasticity Model

Youcai Wu, Ph.D.¹; and John E. Crawford, P.E., M.ASCE²

Abstract: A description and results from validation studies for the Karagozian & Case (K&C) concrete (KCC) model are presented in this paper. This material model is primarily intended for modeling the dynamic responses of RC structural components. It is based on a partially associative plasticity theory and has proven itself capable of replicating most of the key behaviors of concrete, such as those related to hardening, softening, rate effects, confinement, shear dilatancy, and fracture. Three pressure-sensitive, independent strength surfaces are used by the KCC model to capture the variations in hardening and softening behaviors exhibited by concrete. These three strength surfaces are used to compute a failure surface that reflects the influence on the concrete's behavior of the current stress and strain states at a material point. This dynamic form of the failure surface is realized by interpolating between pairs of fixed-strength surfaces on the basis of the value of a damage parameter computed by the KCC model. Partial associativity is introduced in the flow rule so that the magnitude of the computed shear dilation can be calibrated to match test data. Numerical results obtained from both finite-element (FE) and mesh-free formulations are presented to show the excellent performance of the KCC model for concrete responses induced by quasi-static, blast, and impact loadings. DOI: 10.1061/(ASCE)EM.1943-7889.0000952. © 2015 American Society of Civil Engineers.

Author keywords: Concrete; KCC model; Partial associativity; Rate effects; Shear dilatancy.

Introduction

Concrete by itself and in its reinforced form is a common structural material that is used in a wide variety of engineering applications, such as highway and airport pavements, building and bridge constructions, nuclear containment structures, and hardened military facilities. The safety and performance of these structures under blast, impact, and other forms of extreme loadings has been one of the major concerns for designers in recent years. Because of the high cost and difficulty in conducting experiments to evaluate responses to extreme loadings, physics-based numerical analyses are often the only practical way to evaluate the behaviors engendered by these types of loading. As a consequence, physics-based numerical analysis methods have been developed (for both finite-element and mesh-free formulations) that are able to accurately compute the significant behaviors of concrete and the performance of concrete components even in highly damaged states. This is of particular importance to engineers who have been charged with gauging the performance of structures under extreme loadings and mitigating these sorts of risks. For this purpose, having a reliable and effective high-fidelity physics-based concrete constitutive model is crucial to addressing these forms of structural analysis problems.

Modeling Concrete

To realistically predict the behaviors of concrete and RC structures by numerical approaches, the concrete constitutive model must be

able to simulate concrete behaviors over a wide range of circumstances. This includes those exhibited by small material specimens up to full-scale structural systems and their components across a broad array of designs and types of loading. This also includes capturing correctly the relatively peculiar behaviors of concrete as a material, including such key traits as its increasing strength and ductility with increasing confinement pressures and performing effectively even when extensive cracking is present.

However, concrete is a material that is difficult to characterize because of its heterogeneous nature, history-dependent responses, and the profound influence of confinement on its properties. Because of the mesoscale complexities of concrete's behaviors when in highly damaged states, it is impractical to predict the behavior of concrete on the basis of the response of its constituent materials; consequently, concrete constitutive models are generally constituted at a macroscale level as a homogenous material. This readily lends itself to a characterization using a plasticity formulation, which provides a straightforward scheme to capture the basic stress-strain behaviors of concrete as exhibited over a small region of the concrete continuum. These basic behaviors include the significant differences in peak tensile and compressive strengths, prepeak strength hardening (yielding), postpeak softening, enhancements in strength and ductility caused by confinement (i.e., the so-called confinement effect), shear dilatancy, and strain rate enhancement.

Many attempts have been made by researchers to address the heterogeneity of concrete by developing anisotropic concrete constitutive models, such as the ones based on the general framework of the internal variable theory of thermodynamics by Yazdani and Schreyer (1988), on damage mechanics by Papa and Taliencio (1996), and on the framework of multisurface elastoplasticity-damage theory by Meschke et al. (1998). Cofer and Kohut (1994) presented a general nonlocal microplane model to include the effect of crack formation. Hu and Schnobrich (1989) proposed an elastic strain-hardening plastic (nonassociative) model for modeling concrete. Grassl et al. (2002) introduced a nonassociative plasticity model for concrete by using the volumetric plastic strain as

¹Senior Engineer, Karagozian & Case, 700 N Brand Blvd., Suite 700, Glendale, CA 91203 (corresponding author). E-mail: wu@kcse.com

²President, Karagozian & Case, 700 N Brand Blvd., Suite 700, Glendale, CA 91203.

Note. This manuscript was submitted on October 6, 2014; approved on March 2, 2015; published online on May 21, 2015. Discussion period open until October 21, 2015; separate discussions must be submitted for individual papers. This paper is part of the *Journal of Engineering Mechanics*, © ASCE, ISSN 0733-9399/04015051(24)/\$25.00.

hardening parameter. Rabczuk and Eibl (2003) used a strain rate-dependent coupled damage-plasticity model in their simulations of high-velocity impact on concrete structures. However, most of these models are not available in any commercial software; therefore, their application is limited and not readily validated.

Another branch of efforts in concrete constitutive modeling is to treat concrete as a homogeneous material and mimic its behaviors by using a plasticity formulation. The goal of this type of phenomenological model is to reproduce mathematically the macroscopic stress-strain relations for different loading conditions, ignoring the microscopic and mesoscale mechanisms of the concrete's behavior. The multisurface models such as those proposed by Mroz et al. (1967, 1978), Chen (1982), and Malvar et al. (1997) provide an appropriately rigorous means to realize the sort of hardening and softening behaviors observed in concrete with a plasticity model. The shape of these surfaces in the principal stress-pressure plane (PI-plane) is important in characterizing one of concrete's unique features related to differences observed in responses between triaxial extension and compression tests. These differences are captured by such surfaces as those computed by the Ottosen four-parameter model (Ottosen 1977), the Hsieh-Ting-Chen four-parameter model (Hsieh et al. 1982), and the Willam-Warnke five-parameter model (Willam and Warnke 1975).

Homogenous plasticity material models are relatively easier to commercialize and evaluate for accuracy and are more efficient than anisotropic models. Several of these kinds of concrete material model are embedded in widely used numerical analysis codes and are used by many engineering practitioners. In this regard, the commercial software LS-DYNA [Livermore Software Technology Corporation (LSTC) 2014], which is widely applied in analyzing structural responses of concrete structures subjected to extreme loadings (e.g., blast effects loads), offers such concrete constitutive models as the continuous surface cap model (CSCM or MAT159; Murray 2007; Schwer and Murray 1994), the Riedel-Hiermaier-Thomas (RHT) model (MAT272, Riedel et al. 1999), the Winfrith model (MAT084, Broadhouse 1995), and the Karagozian & Case (K&C) concrete (KCC) model (MAT072, Crawford et al. 2011; Malvar et al. 1997).

The KCC Model

Twenty years ago, K&C found that the material models available for simulating the blast responses of RC structural systems and components afforded poor comparisons between the data generated by high-fidelity physics-based (HFPB) models and those measured in precision blast effects tests. This finding led to an extensive R&D (research and development) effort to improve the capability of HFPB models to predict blast effects responses, which leads to the development of the K&C concrete (KCC) model. However, a complete set of theoretical formulations and implementation details has not been published since the model was first introduced in 1997 (Malvar et al. 1997). How to properly select and determine the parameters for the KCC model has never been published either. To help users to better understand and operate the KCC model, the extensive details of its formulation, numerical implementation, and parameter determination are presented in this paper.

The KCC model, which has been embedded in LS-DYNA for more than 10 years, has been extensively used in many applications involving extreme loads and is widely accepted by engineers in the design-analysis community. Karagozian & Case and other KCC model users has performed extensive validation studies to evaluate the capability of the KCC model in both blind (pretest) predictions (ARUP 2009; Elsanadedy et al. 2011; Hansra 2012; Li et al. 2011; Lin et al. 2013) and posttest validation calculations

(Crawford et al. 2011, 2013; Unosson and Nilsson 2006). Karagozian & Case has also extensively studied the capability of other concrete models in LS-DYNA (Crawford et al. 2011, 2012, 2013). These sorts of studies clearly demonstrate the need to carefully verify the capability of a concrete model before using it in a particular application and performing comprehensive studies of its attributes and applicability to particular classes of problems.

The KCC model has also been implemented in DYNA3D (Lin 2005), PRONTO3D (Morrill et al. 1998), FEFLO (Löhner et al. 2002), and other noncommercial analysis codes. To show the unique potential afforded by the KCC model to simulate responses for a variety of complex concrete behaviors, results from a suite of validation studies are presented in this paper to demonstrate this model's capacity to match experimental data for various forms of responses, such as those emanating from quasi-static, blast, and high-velocity impact loads.

The remainder of this paper is organized as follows: The formulations used by the KCC model are presented and followed by their numerical implementation. Then, selection of the parameters for the KCC model is discussed, and results from validation studies are demonstrated afterward. Conclusions are drawn in the last section.

Formulations for KCC Model

Because this paper is focused on explaining the formulations used by the KCC model and their implementation, extended discussions concerning the modeling of various forms of concrete components (e.g., the modeling of their reinforcement or prestressing) are omitted from the paper. This paper is not intended as a tutorial in the modeling of concrete or reinforced concrete components and as such provides little in the way of guidance other than to demonstrate that with sufficient expertise on the part of the modeler, good results can be achieved for a wide range of problems using the KCC model.

Governing Equations

When considering large deformation, the weak form of the equation of motion for a concrete structure can be written in the following updated Lagrangian form:

$$\int_{\Omega_x} \rho \delta \mathbf{u} \cdot \ddot{\mathbf{u}} d\Omega + \int_{\Omega_x} (\nabla_x^S \delta \mathbf{u}) : \boldsymbol{\sigma} d\Omega - \int_{\Omega_x} \delta \mathbf{u} \cdot \mathbf{b} d\Omega - \int_{\partial\Omega_x^t} \delta \mathbf{u} \cdot \mathbf{t} d\Omega = 0 \quad (1)$$

where ρ = density; \mathbf{u} = displacement vector; overhead dot = time differentiation; $\boldsymbol{\sigma}$ = Cauchy stress tensor; ∇_x^S = symmetric spatial gradient operator; \mathbf{b} = body force; \mathbf{t} = traction on the natural boundary $\partial\Omega_x^t$; and Ω_x = problem domain. All variables are evaluated in the deformed configuration.

The evolution of the stress state $\boldsymbol{\sigma}$ is governed by the constitutive laws selected to simulate the concrete's behaviors. In this section, a description is given of the formulations used by the KCC model, which is based on a damage-dependent, partially associative plasticity formulation. This constitutive law is used for modeling the behaviors of concrete because of its ability to comprehensively and efficiently simulate a wide range of concrete behaviors, particularly those associated with the sorts of highly damaged states, which result from penetration, impact, blast, and other sorts of conditions that might cause extreme levels of material damage.

The failure behavior in the KCC model is characterized by a pressure-dependent yield surface $\Upsilon(p, \boldsymbol{\sigma}, \lambda)$ formulated as (Crawford et al. 2011; Malvar et al. 1997)

$$\Upsilon(p, \boldsymbol{\sigma}, \lambda) = \sqrt{3J_2} - \Gamma(p, J_3, \lambda) \leq 0 \quad (2)$$

where $p = -\sigma_{kk}/3 =$ pressure (compression in positive) calculated by the equation of state (EOS), which represents the volumetric responses, and is described in detail in subsequently. The damage parameter λ is used by the constitutive law to represent the effects of the damage imparted to the concrete by the loading, particularly related to hardening and softening. J_2 and J_3 are the second and third invariants of the deviatoric stress tensor $\boldsymbol{\sigma}'$, respectively, and they account for the influence on the material's responses of the deviatoric stress.

$$J_2 = \frac{1}{2} \boldsymbol{\sigma}' : \boldsymbol{\sigma}', \quad J_3 = |\boldsymbol{\sigma}'|, \quad \text{and} \quad \boldsymbol{\sigma}' = \boldsymbol{\sigma} + p\mathbf{I} \quad (3)$$

To capture large deformation finite rotation effects, the Jaumann's objective rate $\boldsymbol{\sigma}^\nabla$ is used in updating stress states

$$\boldsymbol{\sigma}^\nabla = \dot{\boldsymbol{\sigma}} - \dot{\boldsymbol{w}}\boldsymbol{\sigma} + \boldsymbol{\sigma}\dot{\boldsymbol{w}} = \mathbf{C}^{ep} : \dot{\boldsymbol{\epsilon}} \quad (4)$$

with

$$\dot{\boldsymbol{\epsilon}} = \frac{1}{2}(\mathbf{L} + \mathbf{L}^T) \quad (5)$$

$$\dot{\boldsymbol{w}} = \frac{1}{2}(\mathbf{L} - \mathbf{L}^T) \quad (6)$$

$$\mathbf{L} = \nabla_{\mathbf{x}} \dot{\mathbf{u}} \quad (7)$$

where $\dot{\boldsymbol{\epsilon}}$ and $\dot{\boldsymbol{w}}$ = rate of strain tensor and the spin tensor, respectively; \mathbf{L} = velocity gradient; and \mathbf{C}^{ep} = elastoplasticity tensor. Eq. (4) is often rearranged to decouple the material and rotational responses, as follows:

$$\dot{\boldsymbol{\sigma}} = \mathbf{C}^{ep} : \dot{\boldsymbol{\epsilon}} + \mathbf{R} : \dot{\boldsymbol{w}} \quad (8)$$

with \mathbf{R} being the fourth-order rotational tensor defined as

$$R_{ijkl} = (\sigma_{il}\delta_{jk} + \sigma_{jl}\delta_{ik} - \sigma_{ik}\delta_{jl} - \sigma_{jk}\delta_{il})/2 \quad (9)$$

In addition, the strain rate tensor $\dot{\boldsymbol{\epsilon}}$ can be decomposed into an elastic part $\dot{\boldsymbol{\epsilon}}^e$ and a plastic part $\dot{\boldsymbol{\epsilon}}^p$

$$\dot{\boldsymbol{\epsilon}} = \dot{\boldsymbol{\epsilon}}^e + \dot{\boldsymbol{\epsilon}}^p \quad (10)$$

Failure Surface and Strength Surfaces

The functional $\Gamma(p, J_3, \lambda)$ in Eq. (2) defines a failure surface that is a function of the current values computed for a specific set of state variables (p, J_3, λ) , which establishes the strength of the concrete. The failure surface is dynamic, being a function of λ , and is computed by using an interpolative scheme that uses a pair of fixed surfaces defined by the user's input. For the hardening phase of the KCC model, this pair is denoted as the yield and maximum strength surfaces, and for softening, this pair is denoted as the maximum and residual strength surfaces. This may be represented symbolically as follows:

$$\Gamma(p, J_3, \lambda) = \begin{cases} r_f \cdot \Theta(J_3) \cdot [\eta(\lambda) \cdot (\hat{\sigma}_m(p) - \hat{\sigma}_y(p)) + \hat{\sigma}_y(p)] & \lambda \leq \lambda_m \\ r_f \cdot \Theta(J_3) \cdot [\eta(\lambda) \cdot (\hat{\sigma}_m(p) - \hat{\sigma}_r(p)) + \hat{\sigma}_r(p)] & \lambda \geq \lambda_m \end{cases} \quad (11)$$

where the three pressure-sensitive, independent strength surfaces are defined as

$$\hat{\sigma}_i(p) = a_{0i} + \frac{p}{a_{1i} + a_{2i}p} \quad i = m, y, r \quad (12)$$

The parameter λ in Eq. (11) is generally called the damage parameter, which provides the chief mechanism for effecting the changes in strength caused by the distress imparted to the concrete material. λ is a function of the effective plastic strain.

The influence of strain rate on concrete strength is introduced into the KCC model by r_f , the dynamic increase factor (DIF), which is discussed further in the next section. The three independent strength surfaces cited in Eq. (11), $\hat{\sigma}_m$, $\hat{\sigma}_y$, and $\hat{\sigma}_r$, are called the maximum, yield, and residual strength surfaces, respectively (Malvar et al. 1997). The nine parameters defining these surfaces [i.e., a_{0i} , a_{1i} , and a_{2i} in Eq. (12)] are input by the user and are calibrated from experimental data.

The interpolation function $\eta(\lambda)$ in Eq. (11) provides a means to compute a value for the interpolation parameter η , which varies monotonically as a function of the value of the damage parameter λ . The parameter η provides the means to define through interpolation the failure surface used by the KCC model on the basis of the user-defined strength surfaces [i.e., defined in Eq. (12)]. This is done by interpolating between $\hat{\sigma}_y$ and $\hat{\sigma}_m$ surfaces by using values of η from 0.0 to 1.0 if $\lambda \leq \lambda_m$ and between $\hat{\sigma}_m$ and $\hat{\sigma}_r$ surfaces by using values of η from 1.0 to 0.0 if $\lambda \geq \lambda_m$. In other words, this procedure provides a means to compute a dynamically evolving failure surface by interpolating between the yield and maximum surfaces, which mimics a material hardening response and then interpolating between the maximum and residual surfaces, which mimics a material softening response.

As such, strain hardening and softening behaviors are simply and efficiently captured. An example of this $\lambda - \eta$ relationship is shown in Fig. 1. The development of this curve is explained in the "Determination of KCC Model Parameters." For any specific λ , the failure surface interpolation parameter η is calculated as

$$\eta(\lambda) = \eta^\alpha + \frac{\eta^{\alpha+1} - \eta^\alpha}{\lambda^{\alpha+1} - \lambda^\alpha} (\lambda - \lambda^\alpha) \quad (13)$$

where α = index on the (λ, η) input pairs such that $\lambda \in [\lambda^\alpha, \lambda^{\alpha+1}]$.

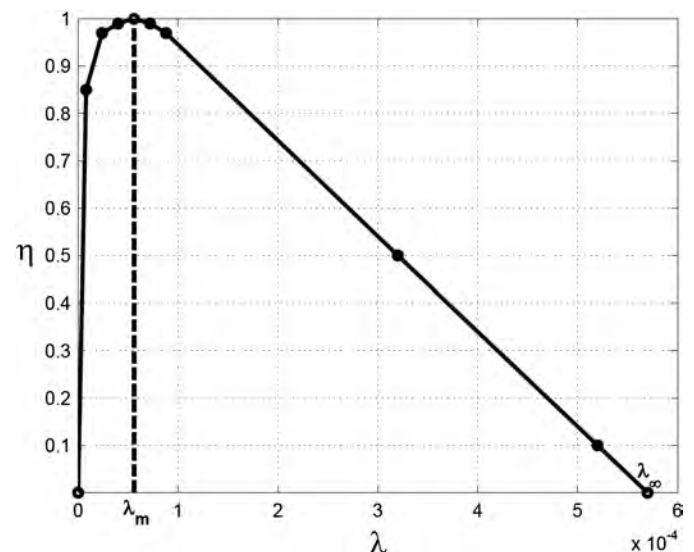


Fig. 1. Failure surface interpolation function $\eta(\lambda)$

Damage Evolution

The evolution of the damage imparted to the concrete is embodied in the damage parameter λ . This parameter reflects the magnitude of the plastic flow computed by the KCC model. By definition, the plastic flow is given as

$$\dot{\epsilon}^p = \dot{\mu} \frac{\partial \varphi(\boldsymbol{\sigma}, p, \lambda)}{\partial \boldsymbol{\sigma}} \quad (14)$$

where the plastic potential $\varphi(\boldsymbol{\sigma}, p, \lambda)$ in the KCC model is expressed as

$$\varphi(\boldsymbol{\sigma}, p, \lambda) = \sqrt{3J_2} - \varpi \Gamma(p, J_3, \lambda) \quad (15)$$

where $\dot{\mu}$ = plasticity consistency parameter; and ϖ = associativity parameter.

The evolution of the damage parameter λ is defined as a function of the rate of plastic strain tensor

$$\dot{\lambda} = h(p) \dot{\epsilon}^p \quad (16)$$

where $\dot{\epsilon}^p = \sqrt{2/3 \dot{\epsilon}^p : \dot{\epsilon}^p}$.

The damage evolution factor $h(p)$ is defined as

$$h(p) = \begin{cases} [1 + p/(r_f f_t)]^{-b_1} / r_f & p \geq 0 \\ [1 + p/(r_f f_t)]^{-b_2} / r_f & p < 0 \end{cases} \quad (17)$$

where b_1 and b_2 = material parameters calibrated from test data.

Capturing the Differences between Extension and Compression

Dependence on the third invariant J_3 of the deviatoric stress $\boldsymbol{\sigma}'$ is introduced into the KCC model to allow it to properly distinguish between triaxial extension and compression behaviors. This dependence is introduced through the functional $\Theta(J_3)$ in Eq. (11).

In the KCC model, $\Theta(J_3)$ uses an expression developed by Willam and Warnke (1975) in the form of

$$\Theta(J_3) = \frac{2(1 - \psi^2) \cos \theta + (2\psi - 1) \sqrt{4(1 - \psi^2) \cos^2 \theta + 5\psi^2 - 4\psi}}{4(1 - \psi^2) \cos^2 \theta + (1 - 2\psi)^2} \quad (18)$$

where the Lode angle θ is determined by

$$\theta = \cos^{-1} \left(\frac{3\sqrt{3} J_3}{2 J_2^{3/2}} \right) / 3 \quad (19)$$

and ψ in Eq. (18) is the ratio between tensile and compressive meridian. The ratio is a function of pressure and can be calculated by (Malvar et al. 1997)

$$\psi = \begin{cases} \frac{1}{2} & p \leq 0 \\ \frac{1}{2} + \frac{3f_t}{2f'_c} & p = \frac{f'_c}{3} \\ \frac{\alpha f'_c}{a_0 m + \frac{2\alpha f'_c}{3a_1 m + 2a_2 m \alpha f'_c}} & p = \frac{2\alpha f'_c}{3}, \alpha \approx 1.15 \\ 0.753 & p = 3f'_c \\ 1.000 & p \geq 8.45f'_c \end{cases} \quad (20)$$

where f'_c = unconfined compressive strength of the concrete. Linear interpolation is applied to obtain the ψ for the pressures falling into the different segments defined in Eq. (20).

Equation of State

Deviatoric and volumetric responses are treated separately in the KCC model. This approach to concrete modeling provides a straightforward means to decouple the shear and compaction behaviors of concrete, which for the classes of problems that are the focus of this model appears to be a wise choice. Although the KCC model provides an excellent means to capture shear dilatancy behaviors, it ignores shear compaction behaviors, which were seen as a needless complication for a model intended to address the response of cementitious materials.

The deviatoric response is determined by the constitutive equation, whereas the volumetric response (i.e., the response to pressure p) is governed by the EOS. A piecewise nonlinear relationship between the volumetric deformation and the pressure and unloading bulk modulus is used for the EOS component of the KCC model, which is calibrated by using test data. This EOS calculates the pressure p as

$$p = p^{\text{EOS}} + K \Delta \epsilon_v^e \quad (21)$$

where $\Delta \epsilon_v^e$ = incremental elastic volumetric strain; p^{EOS} = pressure from the EOS input; and K = bulk modulus. Both p^{EOS} and K are defined by the user as a function of volumetric strain (e.g., as depicted in Fig. 2). The initial bulk modulus is obtained by $K = E/3(1 - 2\nu)$, where Young's modulus E is estimated as $E \approx 4734 \sqrt{f'_c}$, with f'_c in megapascals, and Poisson ratio ν is set as $\nu = 0.19$. Fig. 2 shows the input for the EOS developed for the K&C generic concrete.

Numerical Aspects in Implementation

The KCC model has been implemented for application with both finite-element (FE) and mesh-free formulations. For finite-element formulation, it is available in the commercially available software LS-DYNA (LSTC 2014) and in some less readily available analysis tools such as DYNA3D (Lin 2005), FEFLO (Löhner 2002), and PRONTO3D (Morrill et al. 1998). A coupled FE and mesh-free formulation using the KCC model is also available, which is implemented in the KC-FEMFRE code (Wu et al. 2014a, c). This analysis software was developed by K&C specifically for problems involving extreme distortions.

KC-FEMFRE (Wu et al. 2013, 2014a, c) uses an evolutionary coupling technique whereby the initial analysis model is formulated by using a FE formulation that, as distortions and material damage

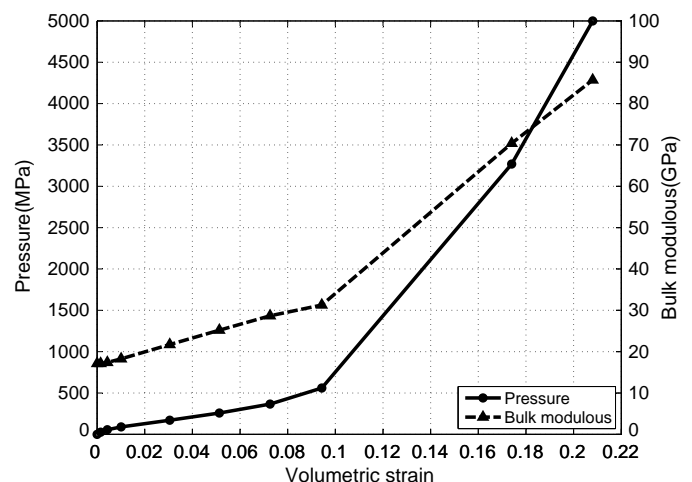


Fig. 2. Equation of state input for the K&C generic concrete

within a region become excessive, is automatically converted to a mesh-free formulation. The mesh-free formulation in the KC-FEMFRE code is based on the reproducing kernel particle method (RKPM) (Chen et al. 1996; Liu et al. 1995).

In this section, the implementation of the KCC model in KC-FEMFRE code is described, which is similar to its implementation in the finite-element formulation.

Plasticity Consistency Parameter

A backward Euler scheme is used to update the state and field variables in the time domain. In a strain driven approach, the displacement vector \mathbf{x}_n , deviatoric stress tensor $\boldsymbol{\sigma}'_n$, plasticity consistency parameter μ_n , and damage parameter λ_n are known from the previous load step, and the incremental displacement $\Delta\mathbf{u}_{n+1}$ is known for the current load step. The \mathbf{x}_{n+1} , $\boldsymbol{\sigma}'_{n+1}$, μ_{n+1} , and λ_{n+1} at the current step are to be determined. Because large deformation is considered, the finite rotation effect needs to be properly treated to preserve objectivity. The classical objective integration algorithm proposed by Hughes and Winget (1980) is used to account for the rotation effect. With the displacement increment $\Delta\mathbf{u}_{n+1}$, the increments of the rate of strain tensor and the spin tensor [given in Eqs. (5) and (6)], denoted by $\Delta\boldsymbol{\varepsilon}$ and $\Delta\mathbf{w}$, are expressed as

$$\Delta\boldsymbol{\varepsilon} = \frac{1}{2}(\mathbf{A} + \mathbf{A}^T) \quad (22)$$

$$\Delta\mathbf{w} = \frac{1}{2}(\mathbf{A} - \mathbf{A}^T) \quad (23)$$

where the gradient \mathbf{A} of the incremental displacement $\Delta\mathbf{u}$ with respect to spatial coordinate \mathbf{x} is calculated through the midpoint rule (Hughes and Winget 1980)

$$\mathbf{A} = \mathbf{H} \left(\mathbf{I} + \frac{\mathbf{H}}{2} \right)^{-1} \quad (24)$$

with

$$\mathbf{H}(\mathbf{x}_L) = \sum_{I=1}^{NP} \mathbf{B}_I(\mathbf{x}_L) \Delta\mathbf{d}_I \quad (25)$$

where \mathbf{x}_L = integration point; NP = number of nodes whose shape function is nonzero at point \mathbf{x}_L ; $\Delta\mathbf{d}_I = [\Delta d_{1I} \ \Delta d_{2I} \ \Delta d_{3I}] =$ coefficient of the incremental displacement of node I ; and \mathbf{B} = gradient matrix given as

$$\mathbf{B}_I(\mathbf{x}_L) = [N_{I,1}(\mathbf{x}_L) \ N_{I,2}(\mathbf{x}_L) \ N_{I,3}(\mathbf{x}_L)]^T \quad (26)$$

where $N_{I,i}(\mathbf{x}_L)$, $i = 1, 2, 3$ = gradient of (or derivatives of FE or mesh-free) shape function of node I evaluated at point \mathbf{x}_L .

The integration of Eq. (8) then becomes (Hughes and Winget 1980)

$$\boldsymbol{\sigma}_{n+1} = \Delta\boldsymbol{\sigma}_{n+1} + \mathbf{Q}\boldsymbol{\sigma}_n\mathbf{Q}^T \quad (27)$$

where \mathbf{Q} = rotational matrix given by (Hughes and Winget 1980)

$$\mathbf{Q} = (\mathbf{I} + \Delta\mathbf{w}/2)(\mathbf{I} - \Delta\mathbf{w}/2)^{-1} \quad (28)$$

The focus here is on the deviatoric stress $\boldsymbol{\sigma}'_{n+1}$ because the volumetric response is governed by the EOS. The deviatoric stress increment $\Delta\boldsymbol{\sigma}'_{n+1}$ is the pure deformation response, and it is determined from the elastoplasticity constitutive relationship. Following the standard return-mapping algorithm (Simo and Hughes 1998), the trial state is defined as

$$\Delta\boldsymbol{\sigma}'_{n+1} = \mathbf{C}:\Delta\boldsymbol{\varepsilon}' \quad (29)$$

$$\Upsilon_{n+1}^{\text{trial}} = \Upsilon(p_{n+1}^{\text{trial}}, \boldsymbol{\sigma}'_{n+1}^{\text{trial}}, \lambda_n) \quad (30)$$

$$\boldsymbol{\sigma}'_{n+1}^{\text{trial}} = \boldsymbol{\sigma}'_n + \Delta\boldsymbol{\sigma}'_{n+1}^{\text{trial}} - p_{n+1}^{\text{trial}}\mathbf{I} \quad (31)$$

where $\Delta\boldsymbol{\varepsilon}'$ = incremental deviatoric strain tensor; p_{n+1}^{trial} = trial pressure predicted by the EOS on the basis of the incremental elastic volumetric strain, which is explained in detail subsequently in this section.

By algebra, the increment of the consistency parameter $\Delta\mu$ can be obtained (see Appendix) by imposing the plasticity consistency condition of $\hat{\Upsilon}_{n+1}^{\text{trial}} = 0$.

$$\Delta\mu = \frac{\Upsilon_{n+1}^{\text{trial}}}{3G + \varpi K(\Gamma_{,p})_{n+1}^{\text{trial}} + (\Gamma_{,\lambda})_{n+1}^{\text{trial}} h(p_{n+1}^{\text{trial}})} \sqrt{1 + 2 \left(\frac{\varpi(\Gamma_{,p})_{n+1}^{\text{trial}}}{3} \right)^2} \quad (32)$$

where G and K = shear and bulk moduli, respectively.

As a result, based on Eq. (16), the increment of the damage parameter λ is given by

$$\Delta\lambda = h(p_{n+1}^{\text{trial}}) = \sqrt{1 + 2 \left(\frac{\varpi(\Gamma_{,p})_{n+1}^{\text{trial}}}{3} \right)^2} \Delta\mu \quad (33)$$

The failure surface Γ can now be updated as

$$\Gamma_{n+1} = \Gamma_{n+1}^{\text{trial}} + (\Gamma_{,p})_{n+1}^{\text{trial}} \Delta p + (\Gamma_{,\lambda})_{n+1}^{\text{trial}} \Delta\lambda \quad (34)$$

with the increment on pressure being calculated by

$$\Delta p = \varpi K(\Gamma_{,p})_{n+1}^{\text{trial}} \Delta\mu \quad (35)$$

This increment on pressure is attributed to plastic flow. If the plastic flow rule is reflective of an incompressible material [e.g., ϖ is 0.0 in Eq. (15)], then plastic flow will not generate any plastic volumetric expansion for additional confinement pressure and, hence, no shear dilation effects. Currently, ϖ takes the following functional form:

$$\varpi = \begin{cases} \varpi_0 / \cosh(\varepsilon_v^e) & \varepsilon_v^e \geq 0 \\ \varpi_0 & \varepsilon_v^e < 0 \end{cases} \quad (36)$$

where ϖ_0 = initial value of ϖ from user input.

By return mapping, the deviatoric stress is scaled back to the yield surface as

$$\boldsymbol{\sigma}'_{n+1} = \frac{\Gamma_{n+1}}{\sqrt{3(J_2)_{n+1}^{\text{trial}}}} \boldsymbol{\sigma}'_{n+1}^{\text{trial}} \quad (37)$$

and the pressure at the current state is calculated as

$$p_{n+1} = p_{n+1}^{\text{trial}} + \Delta p \quad (38)$$

By definition, the increment of the plastic volumetric strain is calculated by

$$\Delta\varepsilon_v^p = \Delta p / K = \varpi(\Gamma_{,p})_{n+1}^{\text{trial}} \Delta\mu \quad (39)$$

and the total plastic volumetric strain is

$$\varepsilon_{v,n+1}^p = \varepsilon_{v,n}^p + \Delta\varepsilon_v^p \quad (40)$$

The damage parameter λ may now be updated by using Eq. (16)

$$\lambda_{n+1} = \lambda_n + \Delta\lambda \quad (41)$$

For the purposes of visualization, the damage parameter is recast into a normalized form called the damage index ϑ , where

$$\vartheta = \frac{2\lambda}{\lambda + \lambda_m} \quad (42)$$

Accordingly, the damage index ϑ equals 0.0 until the concrete material yields, then equals 1.0 when the concrete reaches its maximum strength, and equals 2.0 when the concrete softens completely, reaching the residual strength surface. Fringe plots of the damage index provide an excellent means to visualize the response behaviors exhibited by concrete components, especially when subjected to extreme loadings. Several examples of this sort of plot are given when the numerical examples are presented.

Strength Surfaces

Theoretically, the three pressure-dependent strength surfaces for the KCC model are defined in Eq. (12), and the nine parameters are calibrated from test data. However, because of lack of data, it may be impossible to calibrate the parameters for the whole range of pressure. As a result of the general sparse nature of the test data, several assumptions are built into the KCC model's use of the strength surfaces.

First of all, it is likely that no test data are available for calibrating the maximum strength surface for pressures less than $f'_c/3$ because no damage would occur when the pressure is in this range. Therefore, in the implementation, the maximum strength surface is predefined as

$$\hat{\sigma}_m = \begin{cases} a_{0m} + \frac{p}{a_{1m} + a_{2m}p} & p \geq \frac{f'_c}{3} \\ \frac{3}{2\psi}(p + f_t) & 0 \leq p \leq \frac{f'_c}{3} \text{ or } \lambda \leq \lambda_m \text{ and } -f_t \leq p \leq 0 \\ 3\left(\frac{p}{\eta} + f_t\right) & p \leq 0 \text{ and } \lambda > \lambda_m \end{cases} \quad (43)$$

The segment of the strength surfaces for $p \geq f'_c/3$ is fit by using test data. The segment, where $0 \leq p \leq f'_c/3$, is established by noticing that the ratio between the tensile and compressive meridian is ψ , as defined in Eq. (20). This second segment is determined from tensile meridian data, as data are usually unavailable for the compressive meridian in this range. The tensile meridian in this range is defined as $1.5(p + f_t)$, which passes through data points associated with failure states measured by uniaxial tension ($-f_t/3, f_t$) and triaxial tension ($-f_t, 0$) tests in the $p - \Delta\sigma$ plane. The third segment (i.e., for $p < 0$) is defined by interpolation between the pressure cutoff point ($-\eta f_t, 0$) and $p = 0$ on the second segment, i.e., $(0, 3f_t)$. The pressure cutoff is explained subsequently in this section.

Similarly, the yield strength surface cannot be calibrated for pressure between 0 and $f'_{yc}/3$ (f'_{yc} is the yield strength) because yielding would not even occur when the pressure is in this range. Therefore, the yield strength surface is modified as

$$\hat{\sigma}_y = \begin{cases} a_{0y} + \frac{p}{a_{1y} + a_{2y}p} & p \geq \frac{f'_{yc}}{3} \\ 1.35f_t + 3p\left(1 - \frac{1.35f_t}{f'_{yc}}\right) & 0 \leq p \leq \frac{f'_{yc}}{3} \\ 1.35(p + f_t) & p \leq 0 \end{cases} \quad (44)$$

By investigating test data, it is suggested that the yield surface is approximately the locus of points at $\hat{\sigma}_y = 0.45\hat{\sigma}_m$. Accordingly, the first segment can be determined from test data. The second segment is the linear interpolation between points $(0, 1.35f_t)$ (45% of maximum surface at $p = 0$) and $(f'_{yc}/3, f'_{yc})$ (yielding point), as there are no data to define the yield strength surface directly in this region. The third segment is linear interpolation between the pressure cutoff point ($-f_t, 0$) and $(0, 1.35f_t)$ (45% of maximum surface at $p = 0$). The pressure cutoff here is $-f_t$ rather than $-\eta f_t$ because $\lambda < \lambda_m$ always holds for the yield strength surface.

The residual strength surface $\hat{\sigma}_r$ [e.g., as depicted in Fig. 3(a)] provides the means to model the brittle-ductile transitions that occur as values of confinement stress increase. For very high confinements, concrete may even exhibit hardening behaviors, which the KCC model captures when the residual surface is defined such that at higher pressures it is equal or greater than the maximum surface.

Demonstration of Stress Path Calculation

An example demonstrating the capability provided by the KCC model is given in this section to illustrate the basic features of the model. This example, as shown in Fig. 3, pertains to using a single solid element to compute results for a triaxial compression test with a confinement pressure of 14.0 MPa. The example demonstrates the way that the three independent strength surfaces are used in calculating a particular stress path. These surfaces represent the fit generated by K&C for a generic concrete with an unconfined compressive strength of $f'_c = 45.4$ MPa; values for the parameters of the KCC model for this fit are given in next section.

f_t in Fig. 3 is the tensile strength of the concrete. According to an expression given in ACI 318-95 [American Concrete Institute (ACI) 1995], the concrete's tensile strength f_t may be computed as a function of its compressive strength f'_c as

$$f_t \approx 0.56\sqrt{f'_c} \quad (45)$$

with f_t and f'_c expressed in megapascals.

The stress path response depicted in Fig. 3(d) was computed by using a single solid element [Fig. 3(c)] that is subjected to a triaxial compression (TXC) loading, whose path is depicted in Fig. 3(b). This path starts at the origin and then sequentially passes through points 0, 1, 2, and 3. The loading procedure is as follows:

- From the origin to point 0 (confinement applied): The concrete specimen is hydrostatically compressed to the specified hydrostatic pressure for the peculiar triaxial test, which represents the confinement that this test is to be run at (in this case, 14.0 MPa). Higher values of confinement can dramatically increase concrete strength, as is discussed in the first example and may be inferred by comparing the locations of the intersections with the three strength surfaces of a vertical line through point 0 and the corresponding locations on the $\Delta\sigma$ axis [Fig. 3(b)]. Because point 0 is located on the p -axis, the value of stress difference associated with this state is zero ($\Delta\sigma = 0$). In this situation, the stress difference $\Delta\sigma$ is identical to the J_2 stress invariant in Eq. (3), which equals $\sigma_a - \sigma_r$ [Fig. 3(c)], which is essentially 0 because $\sigma_a = \sigma_r = p$ (the confinement stress).

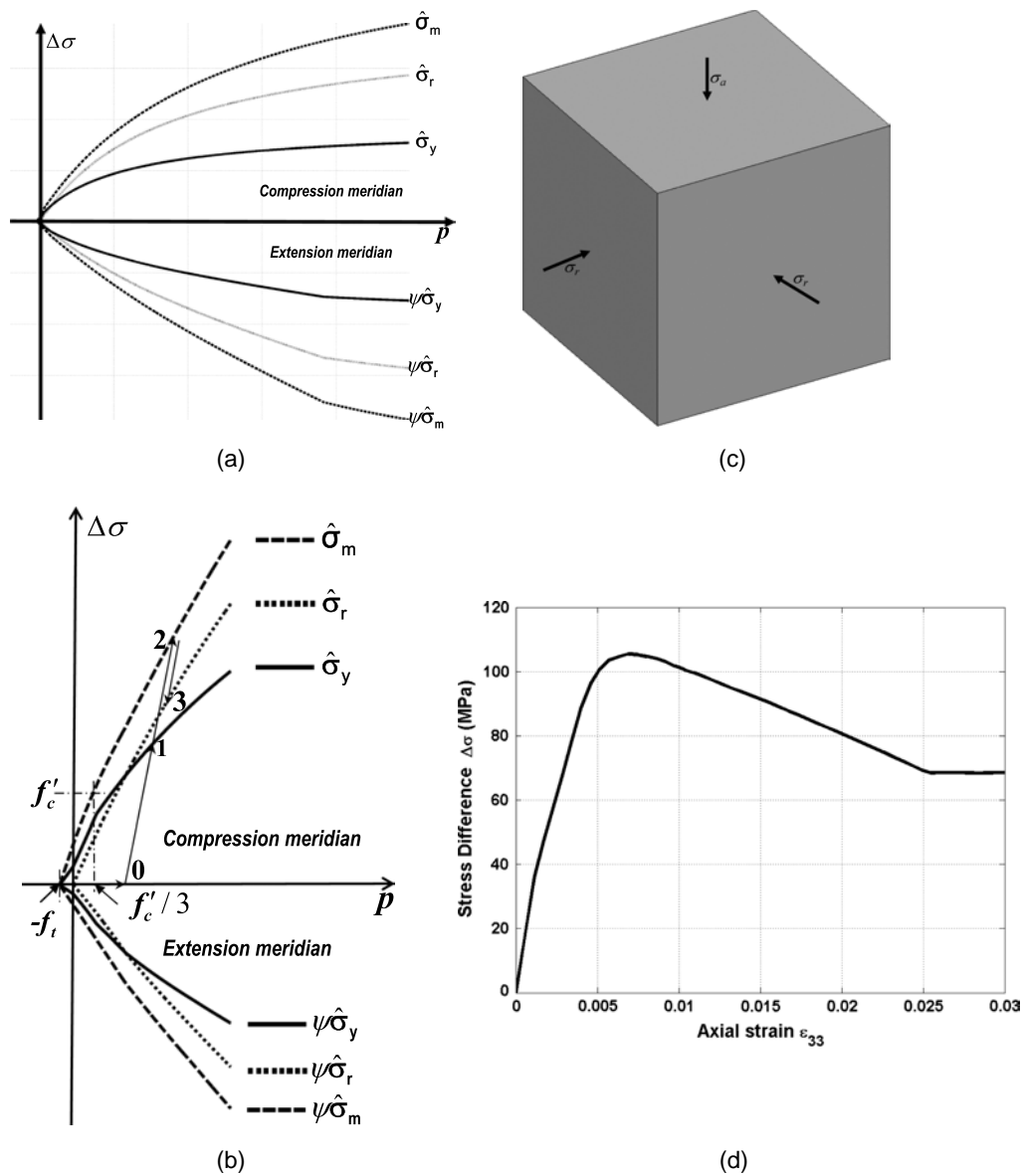


Fig. 3. Example of single element triaxial compression test: (a) strength surfaces in general; (b) details of surfaces near origin; (c) single-solid element used to compute response for stress path shown in Fig. 3(b); (d) resulting stress-strain response for stress path shown

- From point 0 to point 1 (linear elastic response): When σ_a is increased while leaving σ_r unchanged, the stress difference increases. When the stress difference $\Delta\sigma$ reaches point 1, the concrete yields and effective (or deviatoric) plastic strain is induced, and λ starts to increase in value, reflecting the accumulation of damage (i.e., $\lambda = 0$ up to this point).
- From point 1 to point 2 (strain hardening): As the axial stress continues to increase, plastic strain is accumulated. As a consequence, $\eta(\lambda)$ starts to move along the curve defined in the $[0, \lambda_m]$ region in Fig. 1. Between points 1 and 2, the failure surface $\Gamma(p, J_3, \lambda)$ in Eq. (11) is computed by interpolation between the yield and maximum strength surfaces. Once the stress difference reaches point 2, the concrete achieves its maximum strength ($\lambda = \lambda_m$).
- From point 2 to point 3 (softening commences): After reaching its peak strength, as the concrete is further loaded, the stress difference $\Delta\sigma$ decreases (i.e., as the stress path moves towards point 3), at which state the concrete is 100% softened, and its behavior is defined solely by the residual strength surface.

During this phase, $\eta(\lambda)$ varies according to the curve defined in the $[\lambda_m, \lambda_\infty]$ region in Fig. 1, and the failure surface $\Gamma(p, J_3, \lambda)$ is computed by interpolating between the maximum and residual strength surfaces.

Equation of State and Pressure Cutoff

In the KCC model, pressure p is calculated by the EOS according to Eq. (21). The input for the EOS is the relationship between elastic volumetric strain (logarithm) and pressure and elastic volumetric strain (logarithm) and unloading bulk modulus. The elastic volumetric strain at the current step is calculated as

$$\varepsilon_{v,n+1}^e = \ln(V_{n+1}/V_0) - \varepsilon_{v,n}^p \quad (46)$$

where V_{n+1} = current volume; V_0 = original volume; and $\varepsilon_{v,n}^p$ = plastic volumetric strain at the previous step.

The bulk modulus in Eq. (21) is obtained differently for loading and unloading. For loading, it is calculated through pressure-elastic volumetric strain relationship as

$$K^L = \left| \frac{P_{\text{EOS}}^\alpha - P_{\text{EOS}}^{\alpha+1}}{\varepsilon_{v,\text{EOS}}^\alpha - \varepsilon_{v,\text{EOS}}^{\alpha+1}} \right| \quad \varepsilon_{v,n+1}^{e,\min} \in [\varepsilon_{v,\text{EOS}}^{\alpha+1}, \varepsilon_{v,\text{EOS}}^\alpha] \quad (47)$$

where the subscript EOS indicates that the value is taken from the EOS input; and superscript α implies the sequence on the EOS input such that $\varepsilon_{v,n+1}^{e,\min} \in [\varepsilon_{v,\text{EOS}}^{\alpha+1}, \varepsilon_{v,\text{EOS}}^\alpha]$. The loading pressure is the interpolation between p^α and $p^{\alpha+1}$ with $\varepsilon_{v,n+1}^{e,\min}$, which is given as

$$p^L = p_{\text{EOS}}^\alpha - K^L (\varepsilon_{v,n+1}^{e,\min} - \varepsilon_{v,\text{EOS}}^\alpha) \quad (48)$$

The peak compressive elastic volumetric strain $\varepsilon_{v,n+1}^{e,\min}$ in the entire deformation history is defined as

$$\varepsilon_{v,n+1}^{e,\min} = \min(\varepsilon_{v,n}^{e,\min}, \varepsilon_{v,n+1}^e) \quad (49)$$

By definition, $\varepsilon_{v,n+1}^{e,\min} \leq 0$ because logarithmic strain is used. It reaches its minimum value at the peak compression in an unconfined compression test, and it is always zero in an unconfined extension test. The volumetric strain in the EOS input is specified in descending order (i.e., $\varepsilon_{v,\text{EOS}}^{\alpha+1} < \varepsilon_{v,\text{EOS}}^\alpha$), as shown in Table 1.

For unloading, the bulk modulus is computed as

$$K^{UL} = K_{\text{EOS}}^\alpha + \frac{K_{\text{EOS}}^{\alpha+1} - K_{\text{EOS}}^\alpha}{\varepsilon_{v,\text{EOS}}^{\alpha+1} - \varepsilon_{v,\text{EOS}}^\alpha} (\varepsilon_{v,n+1}^{e,\min} - \varepsilon_{v,\text{EOS}}^\alpha) \quad (50)$$

and the unloading pressure is obtained by

$$p^{UL} = p_{\text{EOS}}^\alpha + K^{UL} \Delta \varepsilon_v^e \quad (51)$$

with

$$\Delta \varepsilon_v^e = \varepsilon_{v,n+1}^{e,\min} - \varepsilon_{v,n+1}^e \quad (52)$$

If unloading occurs, $\Delta \varepsilon_v^e$ must be negative because $\varepsilon_{v,n+1}^{e,\min}$ is the minimum value, and the concrete expands when unloading occurs.

Pressure cutoff is enforced on the pressure calculated by the EOS because the EOS would return a very large negative pressure for large volumetric extensions ($\Delta \varepsilon_v^e \rightarrow -\infty$) beyond cracking, which is unphysical. The pressure cutoff is defined as (Malvar et al. 1997)

$$p_c = \begin{cases} -f_t & \lambda \leq \lambda_m \\ -\eta f_t & \lambda > \lambda_m \end{cases} \quad (53)$$

It is noticed that the pressure cutoff is damaged after the concrete reaches its maximum strength surface. The scaled bulk modulus and the corrected shear modulus as defined in Malvar et al. (1997) are used in the plasticity correction [i.e., in Eq. (32) through Eq. (39)].

Table 1. EOS for the K&C Generic Concrete

ε_v	p (MPa)	K (GPa)
0.0	0.0	17.14
-0.0015	25.71	17.14
-0.0043	56.05	17.38
-0.0101	89.99	18.25
-0.0305	170.98	21.72
-0.0513	257.88	25.19
-0.0726	365.87	28.66
-0.0943	559.73	31.28
-0.1740	3,267.88	70.37
-0.2080	4,998.23	85.70

Volumetric Damage

According to Eq. (32), no plastic strain will be accumulated for an isotropic extension loading path because J_2 is always zero no matter how much the tensile pressure is; hence, by Eq. (39), no volumetric plastic strain will be accumulated either. Then, by Eq. (48), the loading pressure in an isotropic extension event could be very high. However, the tensile strength of concrete is usually very low. Therefore, volumetric damage is introduced to correct the unphysical responses that would otherwise be predicted. The failure surface for an isotropic extension loading path is $p = p_c$ and $p < 0$. The yield function in this case is written as

$$f(p) = p_c - p \leq 0 \quad (54)$$

By Taylor expansion

$$f(p_{n+1}) = f(p_n) + \left. \frac{\partial f(p)}{\partial \varepsilon_v^p} \right|_{n+1} \Delta \varepsilon_{v,n+1}^p \quad (55)$$

Material yielding occurs if $f(p_{n+1}) > 0$, and then the classical return mapping algorithm is applied to obtain the incremental volumetric plastic strain. By noticing that $f(p_n) = 0$ is satisfied just before the yielding, Eq. (55) gives

$$\Delta \varepsilon_{v,n+1}^p = \frac{f(p_{n+1})}{\left. \frac{\partial f(p)}{\partial \varepsilon_v^p} \right|_{n+1}} = \frac{p_c - p_{n+1}}{K} \quad (56)$$

where p_{n+1} = pressure predicted by the EOS without enforcing pressure cutoff. Finally, the total effective volumetric plastic strain $\varepsilon_{v,n+1}^p$ is updated as shown in Eq. (40).

Strain Rate Enhancement

Rate Effects Phenomena

Several extensive studies pertaining to the characterization of rate effects and their causes have been conducted by K&C (Crawford et al. 2011; Magallanes et al. 2010; Malvar and Crawford 1998; Malvar and Ross 1998), which provide the basis for the manner in which rate effects are incorporated in the KCC model. This paper presents in the third example results that challenge the fallacy that rate effects can just simply be ignored.

Although a more extensive discussion concerning rate effects is beyond the scope of this paper, a forthcoming paper by Magallanes et al. (unpublished data, 2014) examines the rate effects in detail. This paper shows that the approach used by the KCC model is soundly based and captures well the phenomena associated with both tensile and compressive rate effects observed in material tests and the rate effects phenomena observed in blast effects tests of RC components. Moreover, this study shows that this phenomenon is both real and complex and needs a nuanced approach in its consideration.

Rate Effects Characterization

The strain rate enhancement is important for the KCC model if it is to effectively capture high strain rate events, which has been repeatedly demonstrated in benchmark comparisons with blast effects experiments (Malvar and Crawford 1998; Malvar and Ross 1998). Strain rate enhancement effects are realized through a DIF that modifies the failure surface [cf. Eq. (11)] to reflect apparent changes in strength. The DIF is generally specified as a function of strain rate, either in the form of a curve input by the user or defined internally to the KCC model.

This factor may be defined by using the following formulations. According to Comité Euro-International du Béton (CEB) data (CEB 1990), the compression DIF can be calculated by

$$r_{fc} = \begin{cases} \left(\frac{\dot{\epsilon}}{\dot{\epsilon}_s}\right)^{1.026\alpha} & \dot{\epsilon} \leq 10^6/s \\ \gamma \left(\frac{\dot{\epsilon}}{\dot{\epsilon}_s}\right)^{1/3} & \dot{\epsilon} > 10^6/s \end{cases} \quad (57)$$

with

$$\gamma = 10^{6.156\alpha-2} \quad (58)$$

$$\alpha = \frac{1}{5 + 0.9f'_c} \quad (59)$$

where $\dot{\epsilon}$ = strain rate; $\dot{\epsilon}_s = 3 \times 10^{-5}/s$ = reference strain rate; and f'_c is in megapascals. Magallanes et al. (2010) suggested that the second branch of the strain rate effect showed in CEB data (CEB 1990) should be ignored because of the inertia effect.

According to Malvar et al. (Malvar and Crawford 1998; Malvar and Ross 1998), the tension DIF can be computed as

$$r_{ft} = \begin{cases} \left(\frac{\dot{\epsilon}}{\dot{\epsilon}_s}\right)^\delta & \dot{\epsilon} \leq 1.0/s \\ \beta \left(\frac{\dot{\epsilon}}{\dot{\epsilon}_s}\right)^{1/3} & \dot{\epsilon} > 1.0/s \end{cases} \quad (60)$$

with

$$\beta = 10^{6\delta-2} \quad (61)$$

$$\delta = \frac{1}{1 + 0.8f'_c} \quad (62)$$

where $\dot{\epsilon}$ = strain rate; and $\dot{\epsilon}_s = 10^{-6}/s$ = reference strain rate. Again, f'_c is in megapascals.

Determination of KCC Model Parameters

The KCC model was constructed to afford a wide range of capabilities in capturing phenomena associated with cementitious materials. The model uses many parameters to calibrate its performance so as to produce responses similar to those observed in tests of specific kinds of cementitious materials.

Specifying values for the parameters used by the KCC model may present a daunting task for many users, so a set of parameters for a generic concrete (labeled in this paper as the K&C generic concrete with $f'_c = 45.4$ MPa) has been developed by K&C for use in modeling the behaviors of normal-strength concretes. This set of parameters is labeled as the “default fit.”

Default Fit

The default fit includes 9 parameters defining the strength surfaces, 26 for the failure surface interpolation function, 30 for the EOS, 3 for damage evolution control, and possibly several more for defining the influence of rate effects. However, users are allowed to define their own failure surface interpolation function and EOS (not necessarily 26 and 30 parameters, respectively).

The set of parametric values for the default fit is based on a composite suite of data taken from behaviors observed for several different concrete mixes of similar strength (45.4 MPa) and behavior characteristics. These data were garnered from a variety of tests

and analytic expressions given in the literature (e.g., the expression for Young’s modulus). The development of this fit is quite straightforward for some parameters, whereas for others an extensive series of calibration studies are involved. This effort is documented in other K&C reports and papers (Crawford 2013; Crawford et al. 2011, 2012, 2013; Magallanes et al., unpublished data, 2014). For the most part, the default fit is derived from the concrete behaviors measured in basic tests of cylindrical concrete specimens. Data from tests of simplified structural components [e.g., cylindrical concrete specimens wrapped with carbon fiberreinforced plastic (CFRP)] were used to establish the values for the more ambiguous parameters (mainly those related to damage evolution).

The default fit has been used successfully and extensively by K&C to compute a wide range of results for many different forms of concrete and reinforced concrete components and systems subjected to extreme loads, generally pertaining to blast and impact effects (Crawford et al. 2011, 2013; Magallanes et al. 2010; Wu et al. 2013, 2014b, c). This default fit depicts the sorts of values used for these parameters that have been found appropriate for use with the KCC model. Moreover, because these parameter values have been used successfully to address a broad class of analysis problems, they offer a definitive set of input data for the KCC model. When used with concrete strengths other than that of the K&C generic concrete (45.4 MPa), the scaling procedure described in next subsection may be used to revise the model parameters accordingly.

Strength Surface Parameters

The nine parameters that are used for defining the three strength surfaces for the default fit, as expressed in Eq. (12), are listed in Table 2. These parameters can be scaled to define the strength surfaces for other concretes, as discussed in the next subsection.

Failure Surface Interpolation Function

The 26 parameters that are used for defining the failure surface interpolation function $\eta(\lambda)$, which appears in Eq. (11), are listed in Table 3. This interpolation function was found valid not only for the K&C generic concrete but also for all other concretes examined.

Equation of State

The 30 parameters (i.e., 10 each for elastic volumetric strain, pressure, and bulk modulus) used for defining the EOS for the K&C generic concrete, as was discussed in previous sections, are presented in Table 1. This default set of EOS can be scaled to obtain the EOS for other concretes.

Damage Evolution Parameters

Table 4 lists the values for the damage evolution parameters for the KCC model that have been found to produce meaningful results as gauged by the results produced from several validation studies conducted by K&C (Crawford 2013; Crawford et al. 2011, 2012, 2013). The damage evolution parameters include the b_1 parameter, which controls compression softening; the b_2 parameter, which controls tension softening; and the associativity parameter ϖ , which controls shear dilatancy behavior. These parameters, which can have a marked influence on responses, appear in Eqs. (15)

Table 2. Strength Surface Parameters for the K&C Generic Concrete

Parameters	Yield surface	Maximum surface	Residual surface
a_0 (MPa)	10.13	13.41	0.0
a_1	0.625	0.4463	0.4417
a_2 (MPa ⁻¹)	0.005676	0.001781	0.002608

Table 3. Failure Surface Interpolation Function for the Default Fit

λ	η
0.0	0.0
8.0×10^{-6}	0.85
2.4×10^{-5}	0.97
4.0×10^{-5}	0.99
5.6×10^{-5}	1.00
7.2×10^{-5}	0.99
8.8×10^{-5}	0.97
3.2×10^{-4}	0.50
5.2×10^{-4}	0.10
5.7×10^{-4}	0.00
1.0	0.00

Table 4. Nominal Values for Damage Evolution Parameters

Parameter	Value	Comment
b_1	1.60	Per Eq. (67), this value for an element size of 60 mm
b_2	1.35	Per Eq. (68), this value for an $f'_c = 37.7$ MPa, and $w_{Lz} = 50$ mm
ϖ	<0.5	For high- and ultra-high-strength concretes with fine aggregate
	0.50.75	For poorly confined concrete components or concretes without coarse aggregate
	0.80.9	For well-confined, normal-strength concrete components

and (17). The values selected for these parameters and their influence on the response should be carefully studied by the user. The influence of element size on the b_1 and b_2 parameters and a discussion pertaining to the selection of ϖ are given subsequently in this section.

Remarks on the Default Fit

The parameters for the default fit have changed little because the KCC model was first publically introduced in a 2001 implementation in LS-DYNA. These changes mostly involved developing expressions for the model's parameters that control tensile and compressive softening that reflect the influence of element size on the results and developing closed form expressions to capture the effects of strain rate. Also, considerable effort has been expended to provide a more definitive value for the shear dilatancy parameter ϖ , which is crucial to determining the influence of steel reinforcement and CFRP wrap in terms of their ability to enhance concrete strength and ductility caused by confinement effects.

Several of the example problems shown in the next section demonstrate the marked influence of parameter selection on the responses computed. For example, the values selected for parameters ϖ , b_1 , and b_2 are often crucial to correctly predict results for highly damaged and/or well-confined RC components. Selection of both b_1 and b_2 are effected by element size, and expressions for their calculation are given subsequently in this section. The selection of an appropriate ϖ is quite challenging and is particularly important in effectively calculating the capacity and capability provided by well-reinforced concrete components because it plays a crucial role in determining the level of confinement generated as the concrete expands in volume because of cracking. Unfortunately, the functionality [Eq. (36)] associated with ϖ is not constructed well, is still in a state of flux, and tests germane to its selection are sparse. However, recent studies by K&C have shown considerable promise in the functionality represented by the KCC model for well-confined concrete components using values of ϖ approximately 0.90. Some results from these studies are presented in the second

example and by Crawford (2013). These studies also showed the remarkably poor results that are generated by the KCC model when the shear dilatancy characterization is not selected appropriately, which has been the case with some users of the KCC model.

Because the KCC model gives the user a great deal of flexibility in its operation (i.e., its ability to adapt itself to fit a broad range of behaviors of cementitious materials), it is not surprising that the default fit is not universally applicable. Although the default fit produces reasonable results in many situations, it is important for modelers to realize that it is their responsibility to select the appropriate input for the KCC model. Moreover, to effectively use a material model with this much capability, the user should have an extensive knowledge of the phenomenology exhibited in both standard material tests (i.e., those performed with small plain concrete specimens) and in precision tests of RC components and of the features of the KCC model that are related to particular aspects of this phenomenology. This is crucial to effectively using a constitutive model like the KCC model, which is intended to allow a skillful user to simulate the actual behaviors observed, particularly under extreme loadings.

Although the parameter values cited in this section have shown themselves to produce reasonable results in many applications, they do not represent a "be all, end all" resolution to the need for the user to exercise caution in using a material model with as much capability and flexibility as the KCC model.

Scaling of Parameters

It is highly unlikely that enough data will be available to objectively determine values for all the parameters of the KCC model for any particular concrete. In K&C's development efforts, it was found that a reasonable approximation of the fit for another concrete—for instance, one with a compressive strength different from that of the K&C generic concrete (i.e., as represented by the default fit)—could be obtained by scaling the default-fit parameters of the KCC model.

Thus, to develop a fit for another concrete with a known unconfined compressive strength of $f'_c{}^{\text{new}}$, its strength surfaces and EOS parameters are obtained by scaling the analogous parameters for the known fit (e.g., the default fit). This is done as follows, assuming the strength surfaces for the new concrete are expressed as

$$\hat{\sigma}_i^{\text{new}} = a_{0i}^{\text{new}} + \frac{p}{a_{1i}^{\text{new}} + a_{2i}^{\text{new}} p} \quad i = m, y, r \quad (63)$$

Then the strength surface parameters are given in terms of another concrete (i.e., old concrete whose strength surface parameters a_{ji}^{old} $j = 0, 1, 2; i = m, y, r$ are known) as

$$a_{0i}^{\text{new}} = \phi a_{0i}^{\text{old}} \quad a_{1i}^{\text{new}} = a_{1i}^{\text{old}} \quad a_{2i}^{\text{new}} = a_{2i}^{\text{old}} / \phi \quad (64)$$

where the scaling factor ϕ is

$$\phi = \frac{f'_c{}^{\text{new}}}{f'_c{}^{\text{old}}} \quad (65)$$

and $f'_c{}^{\text{old}}$ is the unconfined compressive strength of the concrete whose strength surfaces are known.

To reflect changes in concrete strength for the equation of state, the volumetric strain component is assumed to remain unchanged. Because Young's modulus of a concrete is a function of the square root of the unconfined compressive strength f'_c , the bulk modulus and pressure for the EOS (shown in Fig. 2) are scaled as follows:

$$p^{\text{new}} = \sqrt{\phi} p^{\text{old}} \quad K^{\text{new}} = \sqrt{\phi} K^{\text{old}} \quad (66)$$

The parameter scaling functionality is very helpful for KCC model users because by using it, users only need to know f'_c (the strength of their concrete) to generate a complete set of KCC model parameters that can approximate the behavior of their concrete. In LS-DYNA, this calculation is done internally by the KCC model so that only the new value for f'_c needs to be input and the other KCC model parameters are automatically generated.

The failure surface interpolation function used for the default fit seems to work well for all the normal weight concretes that K&C has investigated; therefore, no scaling for the failure surface interpolation function is used. However, although this function seems to work for a wide range of concrete strengths, some forms of cementitious materials (e.g., mortar, grout) may not be so well modeled. Similar concerns arise for the selection of the damage evolution parameters, especially as influenced by aggregate size, moisture content, and different forms of concrete (e.g., high-strength and ultra-high performance concretes). In these instances, more fundamental changes in the KCC model parameters may be needed. Some of these other fits for cementitious materials are developed by Magallanes et al. (2010; unpublished data, 2014).

Regularization of Damage Evolution Parameters

Concrete under little to moderate confinement exhibits strain softening; therefore, mesh dependence is unavoidable if no treatment is taken to mitigate it. Three parameters are combined in the KCC model to control the damage evolution: b_1 , b_2 in Eq. (17), and ϖ in Eq. (15). b_1 controls compressive damage evolution, b_2 controls tensile damage evolution, and ϖ is the associativity parameter, which also controls volume expansion.

According to Crawford et al. (2011), to regularize the compression softening, b_1 can be approximately estimated as

$$b_1 = 0.0135h + 0.79 \quad (67)$$

where h = characteristic length of the element in millimeters.

According to CEB data (CEB 1990), b_2 can be approximated by

$$b_2 = (1.4 \times 10^{-4} w_{lz}^2 - 0.039 w_{lz} + 3.06)(0.516 - 8.4 \times 10^{-5} f'_c + 0.014 f'_c) \quad (68)$$

where w_{lz} = localization width in millimeters, which is usually three times the maximum aggregate size; and f'_c is the concrete strength in megapascals.

The regularization of b_1 by using Eq. (67), related to its dependence on element size, was obtained by fitting numerical responses to a set of uniaxial compression test data (for a specific concrete). To this point, the manner of computing b_1 was found to be effective in capturing the data from other compression tests.

In contrast, the b_2 regularization is obtained by fitting the numerical fracture energy computed by the KCC model for tension tests to the data generated for various concretes. Therefore, there is no explicit mesh-size dependence that has been developed by K&C, although as of yet more research concerning the specification of the b_2 parameter is ongoing. However, the importance of this might be mitigated by assessing whether the values selected for the parameter are important to the problem at hand. Such guidance is true for all of the damage evolution parameters (b_1 , b_2 , and ϖ), which becomes important only in certain classes of problems.

Although the influence of element size on the selection of ϖ is not so deterministic, element specification (size and discretization) does play a role, as demonstrated in the second example. This is driven by the level of localization associated with the confinement

effects that might result from the shear dilation generated by the ϖ value chosen.

Modeling Shear Dilatancy

The associativity parameter ϖ in Eq. (15), which is the parameter that governs the volume expansion, can have a substantial influence on the structural responses when confinement effects are present. For instance, the behaviors exhibited by RC columns wrapped with CFRP and the capability of an analysis to predict them are strongly influenced by the behaviors represented by ϖ , as shown in the second example.

The values selected for ϖ in situations where shear dilatancy is an important factor in the types of responses to be modeled may be critical to achieving an appropriate result. This was the conclusion of a study conducted by Crawford et al. (2013) of the lateral response up to failure of RC columns wrapped with CFRP.

ϖ plays a central role in determining the proportioning between volumetric and deviatoric components of plastic strain. A value of $\varpi = 1.0$ gives an associative plasticity, in which the normal to the failure surface defines the proportionality. In contrast, a value of $\varpi = 0.0$ provides a Prandtl-Reuss form of plasticity, and plastic volume strain is precluded. A partially associative formulation is invoked for $0.0 < \varpi < 1.0$.

The ϖ parameter provides a means to capture the concrete's expansion (shear dilation) as it cracks, which in turn, if sufficient confinement reinforcement is provided, causes a marked increase in the confinement stress in the concrete and thus adds to its strength and ductility. Values of ϖ between 0.50 and 0.90 have been found effective in previous studies by K&C.

According to Crawford et al. (2011), the suggested value for a well-confined concrete component is 0.90. This value for ϖ was developed by using a set of test data pertaining to plain concrete components that are 762 mm in height with various cylindrical and rectangular cross sections; some components were wrapped with different amounts of CFRP. These tests and their use to develop an appropriate value for ϖ are documented in Crawford et al. (2011). For situations in which confinement pressures are not affected by shear dilatancy, the value selected for ϖ is not so important. This is demonstrated by the results for the third problem, which show that in situations in which confinement is low, the value of ϖ has little influence on the results. In marked contrast, the results shown in the second example are profoundly influenced by shear dilatancy and as a result by the value of ϖ selected.

Numerical Applications

In this section, the KCC model is applied in solving various experimental problems concerning quasi-static, blast, and impact loadings. The problems are analyzed by either the finite-element method, as provided in LS-DYNA, or the coupled finite-element and mesh-free formulation (Wu et al. 2013, 2014c), as implemented in KC-FEMFRE (Wu et al. 2014a). The KC-FEMFRE code provides the capability of evolutionarily coupling the finite-element and reproducing kernel (RK) (Chen et al. 1996; Liu et al. 1995) formulations.

In LS-DYNA, the concrete is discretized by one-point Gauss quadrature integrated solid elements, viscous-type hourglass control is applied to mitigate the effect of zero-energy modes, and erosion is used to remove highly distorted elements. The solutions are compared for various concrete models, including MAT072, MAT084, MAT159, and MAT272. In contrast, neither hourglass control nor erosion is used by KC-FEMFRE. In KC-FEMFRE, the simulation starts with a pure finite-element discretization and

evolves into a mesh-free discretization in portions of the model where the concrete material damage reaches a specified threshold [e.g., a value of η less than 0.05 for $\lambda > \lambda_m$, or a value of 1.98 for ϑ in Eq. (42)]. In KC-FEMFRE, the stabilized conforming nodal integration (SCNI) (Chen et al. 2001, 2002) is used, so hourglass control is not needed because SCNI provides better stability than single-point Gauss quadrature.

The default fit for the parameters of the KCC model is used for the analysis of the application problems given in this section. In some instances, the strength surfaces and EOS are scaled according to Eqs. (64) and (66), respectively, if the concrete's strength f'_c is other than 45.4 MPa of the K&C generic concrete on the basis of which the default fit was developed. Strain rate enhancement is activated and defined according to Eqs. (57) and (60), except in the first two problems because they concern quasi-static loadings.

Problem 1: TXC

As shown in Fig. 4, a plain concrete cylinder with a diameter of 152.4 mm and a height of 304.8 mm is used to perform a series of TXC. The cylinder is discretized by using approximately cubic solid elements with a side dimension of approximately 20.3 mm. For loading, confinement pressure is applied to the side and ends of the cylinder, and then the top surface is moved downward at a constant velocity. The concrete has an unconfined compressive strength of $f'_c = 45.4$ MPa. $b_1 = 1.06$, $b_2 = 1.35$, and $\varpi = 0.50$ are used in the simulation.

LS-DYNA is used to compute the responses for these TXC tests, which are conducted for various values of confining stress. The confinement pressure (as surface traction) is applied gradually to the exterior of the model over the first 50 ms to inhibit wave propagation noise, and afterward the top surface is pushed down at a velocity of 76.2 mm/s. The bottom surface is completely fixed, and the top surface is constrained laterally.

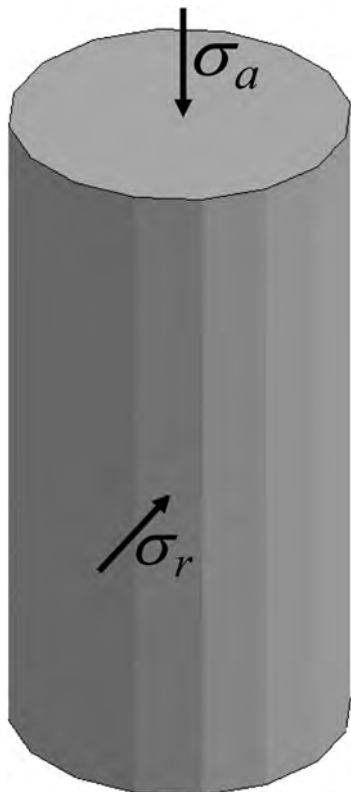


Fig. 4. Problem 1: specimen for TXC tests

Plots of axial strain versus stress difference computed by the model for confinement pressures of 0.0, 7.0, 14.0, 20.0, and 34.0 MPa are presented in Fig. 5. In Fig. 5(a), the solid lines represent computed results, and dashed lines represent test data (Crawford et al. 2011). The numerical results show reasonable agreement with the test data across all levels of confinement. The prepeak yielding and hardening (up to peak) and postpeak softening behaviors are all captured by the model. Transition from brittle to ductile behaviors is observed as confinement pressure is increased. Fig. 5(b) compares the solutions obtained with various concrete constitutive models for the case in which the confinement pressure is 14 MPa. The prediction from MAT072 matches test data fairly well in capturing the peak strength and residual strength; MAT159 and MAT272 underpredict the confinement effect, whereas MAT084 seems to capture the peak response, but it softens rapidly to its residual strength, which is much lower than the experimental observation.

In this situation, the associativity parameter ϖ for MAT072 has very limited influence on the confinement effects because confinement is applied as explicit pressure, and it remains the same whether the concrete dilates or not. The axial strain plotted is the

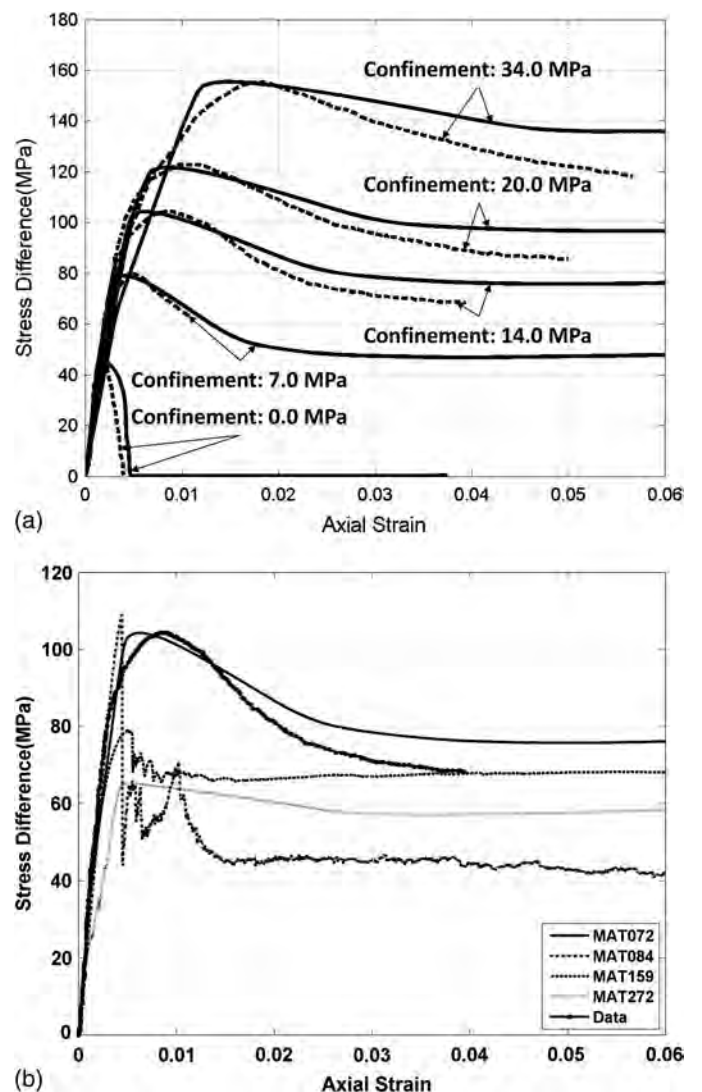


Fig. 5. Problem 1: stress-strain responses for TXC tests: (a) by MAT072 with various confinements; (b) by various concrete models with 14 MPa confinement

difference between the total engineering axial strain and the engineering axial strain induced by the confinement pressure. The stress difference is the difference between the engineering axial stress σ_a and the confinement pressure σ_r (Fig. 4).

Problem 2: Reinforced Concrete Columns Subjected to Lateral Loads

A set of laboratory tests of full-scale RC columns were conducted at the University of California at San Diego (UCSD) for investigating the influence of CFRP wrap on their lateral resistance. The test setup and LS-DYNA model is depicted in Fig. 6. The RC column has a square cross section of 355.6×355.6 mm and a clear height of 3,276.6 mm. For the Gr.60 reinforcement, eight #8 (diameter = 25.4 mm) vertical rebars are used with #3 ties (diameter = 9.5 mm)

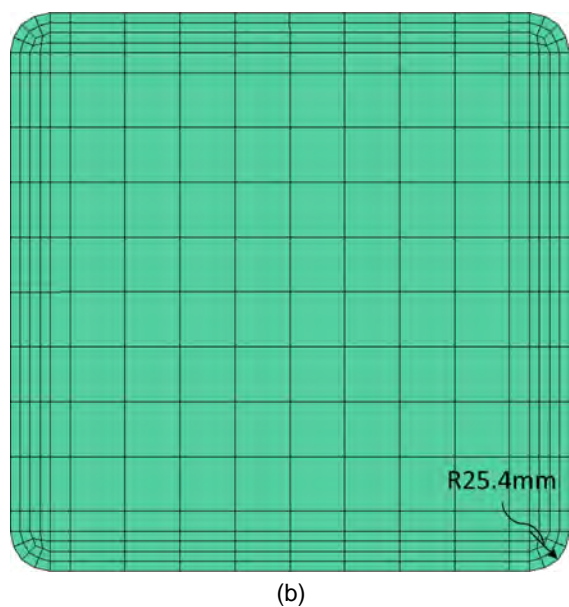
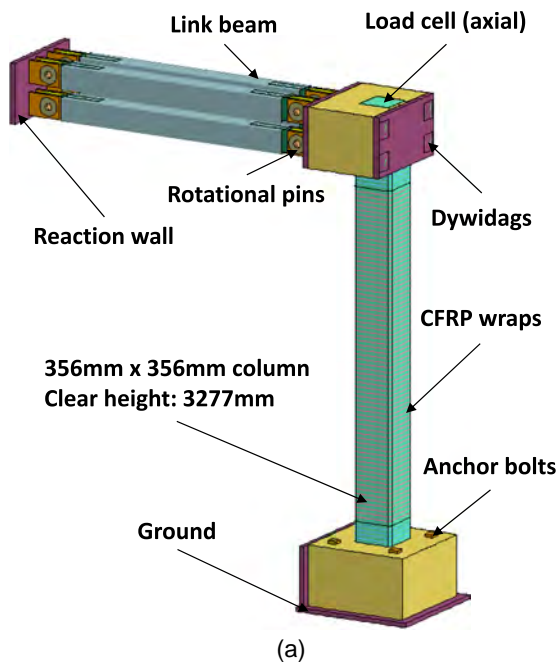


Fig. 6. Problem 2: discretization of RC column tests: (a) isometric view; (b) cross section

at 323.9-mm spacing. Two, six, zero, and four layers of CFRP were applied to enhance the column's response for Tests 2, 3, 4, and 10, respectively. The Young's modulus of the CFRP is 78.6 GPa, and its ultimate strength is 896.6 MPa.

The concrete is modeled with approximately cubic solid elements (38 mm on a side). However, to properly capture the confinement effect exerted by the CFRP wrap, the actual rounding of the column's corners is discretized with finer elements, as shown in Fig. 6(b). The compressive strength of the concrete is 38.6 MPa. In accordance with Eq. (67), $b_1 = 1.28$ for the core elements, $b_1 = 0.98$ for the edge elements, and $b_1 = 0.92$ for the corner elements, whereas in accordance with Eq. (68), $b_2 = 2.02$.

On the basis of the study described in the previous section "Determination of KCC Model Parameters," the dilatancy factor $\varpi = 0.90$ is used to compute responses for Tests 2, 3, and 10 because the CFRP wrap acts as a kinematic constraint, producing a high-level confinement. For Test 4 (i.e., in which no CFRP is present), $\varpi = 0.75$ is used. The use of this value (i.e., as compared to 0.90), as shown in Fig. 7(b), has no influence on the response because little in the way of confinement constraint is afforded by the steel reinforcement present. However, the value for ϖ and the level of shear dilatancy associated with it does have a great influence on the results for the other tests, as shown in a recent K&C paper (Crawford et al. 2013).

In the test, an approximately uniform pressure is applied on the front face of the column to initiate the lateral responses. Before this pressure is applied, an axial load of 445 kN is applied (i.e., to simulate the actual gravity load as if the column were embedded in a building) to the top of the column, which is constrained afterward to not move. Displacements at the reaction wall and the ground are fixed.

The load-deflection responses measured and computed for these tests are presented in Fig. 7. As shown Fig. 7(b), the numerical results obtained with MAT072 reasonably capture well the CFRP failure observed in the tests and the strength and ductility enhancements afforded by the CFRP related to the shear dilatancy exhibited by the concrete. If the associativity factor were chosen as $\varpi = 0.50$, then no CFRP failure would have occurred in the numerical analyses and the post peak response would show considerably less resistance, if any.

The key mechanism of the phenomena exhibited by wrapped columns of this size is that the dilation imparted to the concrete produces tension in CFRP wraps, which in turn applies confinement to the concrete. To capture this phenomenon, the shear dilation of the concrete must be captured appropriately, which is why the associativity parameter must be set to an appropriate value, in this instance $\varpi = 0.90$ for CFRP-wrapped columns (so that enough dilation is generated).

The influence of CFRP (Tests 2, 3, and 10) compared with no CFRP is profound, as shown in Fig. 7(a). As demonstrated in this figure, the more layers of CFRP wrap used, the higher the ductility achieved. These tests also indicate the amount of CFRP needed to prevent the column's failure in tension [e.g., the sudden release of the axial force in Fig. 7(a) caused by CFRP failure]. To capture this failure represents a key test of a concrete constitutive model with regard to its effectiveness in capturing the influence of CFRP on RC column response. Also important in these tests is the marked enhancement in the axial resistance provided by the column, as illustrated by the axial response depicted in Fig. 7(a). This occurs because of the fixity used at its supports. Although both of these phenomena are captured fairly well by the KCC model [Fig. 7(b)], this is not true for many other concrete models (Crawford et al. 2013), which makes their application to such problems suspect.

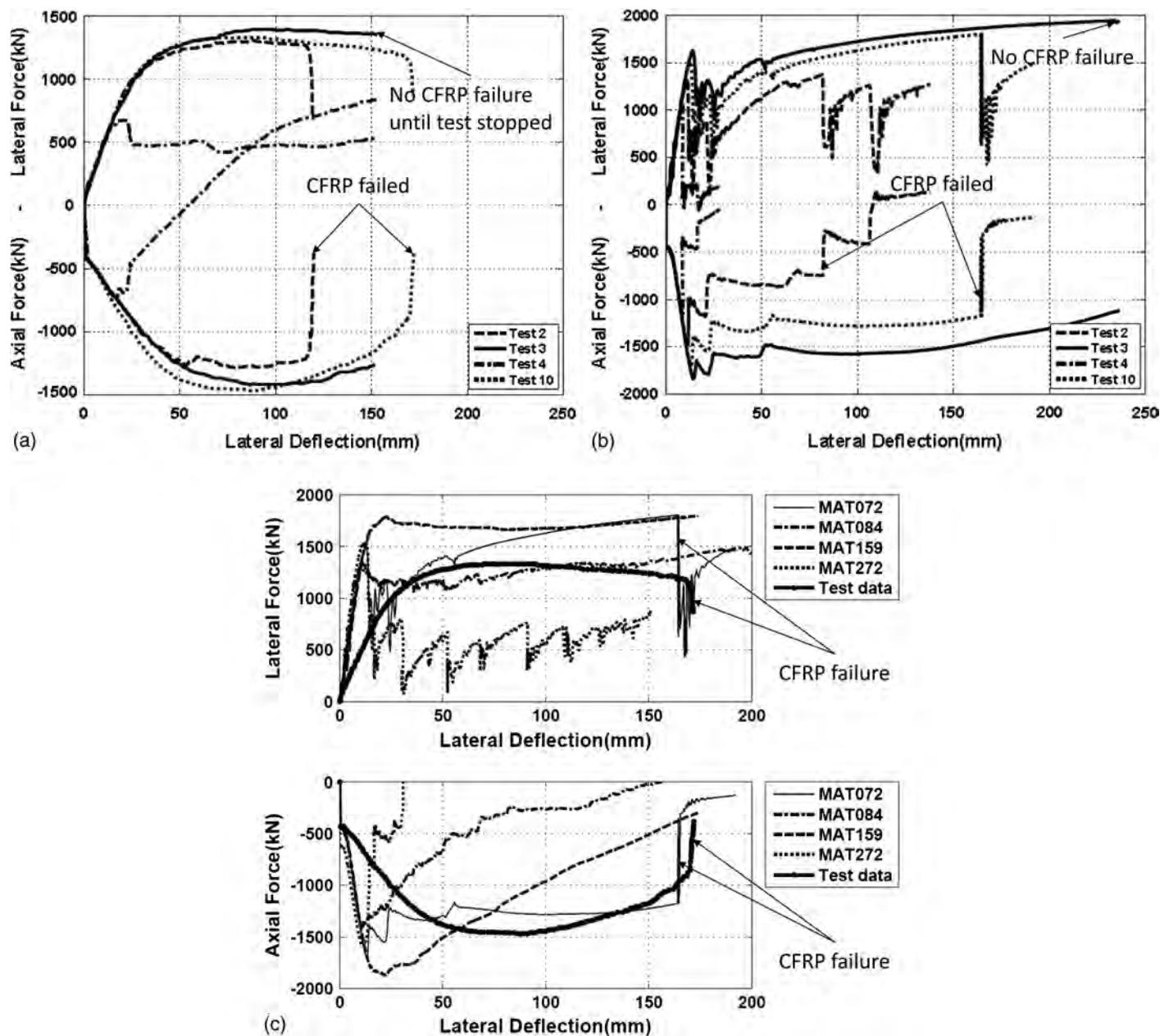


Fig. 7. Problem 2: vertical and lateral resistances for RC columns: (a) test results; (b) numerical results by MAT072; (c) Test 10 results from various concrete models

Although the force-deflection responses could be better, the extensive studies conducted by K&C for this problem (Crawford et al. 2011) indicate that responses are quite sensitive to the discretization at the column's corners, which makes it somewhat impractical to improve on these results because a lot of elements are already present. However, because the most important phenomena exhibited in these tests are captured (i.e., the enhancement on both strength and ductility induced by CFRP wraps and the failure of the CFRP), these analyses were deemed to successfully capture the key responses of these columns.

Fig. 7(c) shows the comparison of the numerical solutions with various concrete constitutive models for Test 10 (column wrapped with four-layer CFRP). Only MAT072 predicts the failure of CFRP, which was also observed in the test. This immediately tells that the other models cannot be used in a design calculation, because they would not be able to predict how many CFRP wraps are needed. In the predicted responses, MAT084 captures the peak

force correctly but cannot predict the CFRP failure and the increase of ductility caused by CFRP wraps (axial force drops quickly). MAT159 predicts a much higher load capacity in both shear and axial directions and cannot simulate the failure of CFRP either, whereas MAT272 seems to capture the peak force correctly, but it softens very rapidly, i.e., no gain on ductility at all although the column is wrapped with four-layer CFRP.

Problem 3: RC Slab Subjected to Blast Loadings

As shown in Fig. 8, a reinforced concrete slab is used to examine the capability of the KCC model in capturing structural responses for a blast loading. The slab has a thickness of 102 mm, width of 857 mm, and height of 1,626 mm (clear = 1,321 mm). The slab is reinforced by #3 rebars. The unconfined compressive strength of the concrete is 34.5 MPa, and the reinforcement is Gr.60 steel.

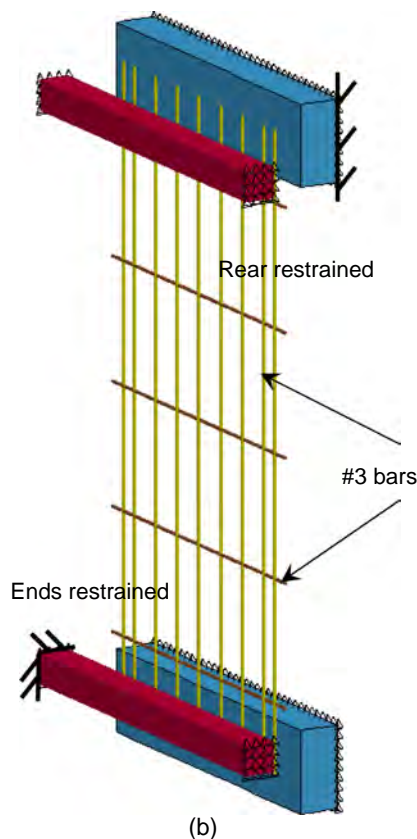
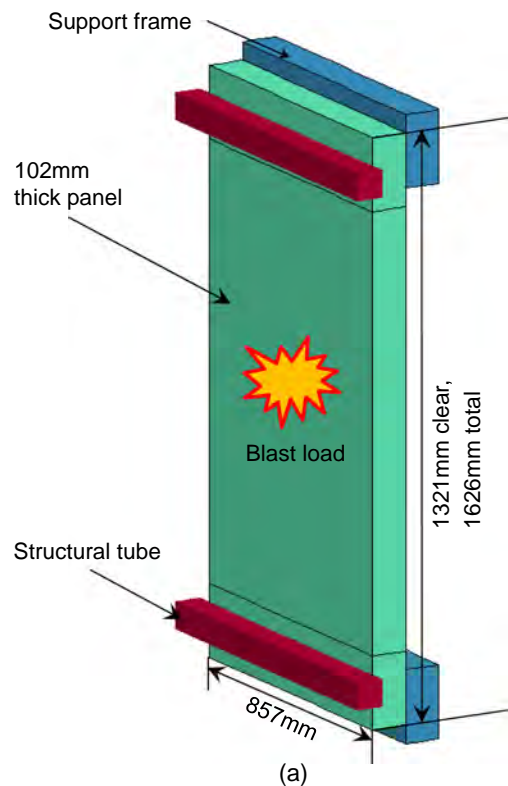


Fig. 8. Problem 3: test setup of RC slab test and analysis: (a) dimensions; (b) boundary conditions

The concrete in the slab is discretized by approximately 25.4 mm cubic solid elements, and the reinforcement is modeled by beam elements sharing nodes with the concrete. The two ends of the slab are held in place [Fig. 8(a)] by a support system composed

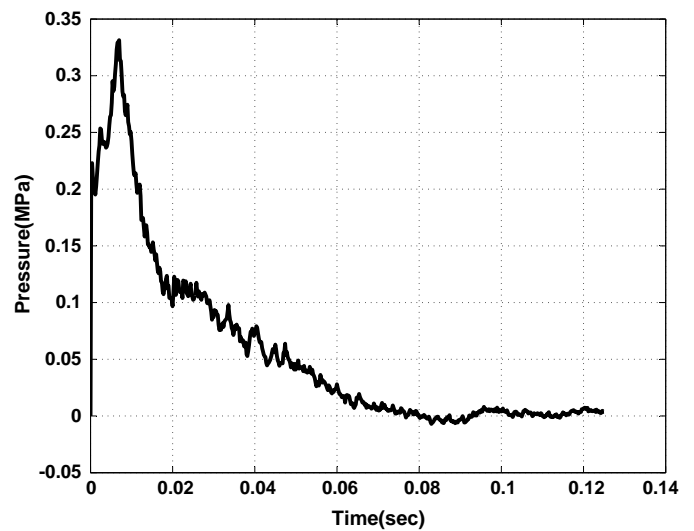


Fig. 9. Problem 3: pressure history for RC slab test

of steel structural tubes placed against the front face and a support frame against the back face of the slab near its edges. Contact interfaces are defined between the slab and the structural tubes and support frames, and the coefficient of friction (COF) is 0.4. The recorded pressure history as shown in Fig. 9 is applied uniformly over the front face of the slab for the blast loading.

The results for two sets of damage evolution parameters are shown. One set represents the default set, i.e., $b_1 = 1.60$, $b_2 = 1.35$, and $\varpi = 0.50$. The other set, designated as the “adjusted fit,” is a set of parameters that was determined in accordance with the discussions in the section of “Determination of KCC Model Parameters” (i.e., $b_1 = 1.12$, $b_2 = 1.96$, and $\varpi = 0.75$). The Gr.60 reinforcement is modeled by using a von-Mises piecewise linear plasticity model.

Fig. 10 compares the numerical results obtained by using LS-DYNA and the experimental data (<http://sce.umkc.edu/blast-prediction-contest/home.html>). In Fig. 10(a), the legend “With Rate” stands for the calculation using the default set parameters with strain rate enhancement, whereas “Without Rate” indicates that the strain rate enhancement is not activated although the same parameters are used. The results designated as “Adjusted” are those computed by using the adjusted fit as previously mentioned. The same strain rate effects, as used for the “With Rate” results, are used. As shown, the better characterization used for the softening (i.e., the adjusted values used for b_1 and b_2) improves the results.

As shown in Fig. 10(a), the strain rate enhancement has a significant impact on the computed responses for MAT072. On this subject, when rate effects are included, the deflection matches the test data very well; otherwise, a large discrepancy exists. This is quite significant because although there may be considerable controversy related to the nature and causes of rate effects, these results are quite telling as to its actual existence.

The responses obtained with MAT072, M084, MAT159, and MAT272 are compared in Fig. 10(b). Both MAT072 and MAT159 calculate the residual deflection correctly, but they both miss the peak deflection; on the other hand, both MAT084 and MAT272 predict very stiff responses, and they both miss the peak and residual displacements.

The results for Problem 3 (in which high strain rates exist and rate effects are included in the KCC model), when viewed in conjunction with those for Problem 2 (in which rate effects are ignored because of the quasi-static level) reinforces the notion that considering rate effects correctly is important. In other words, the KCC

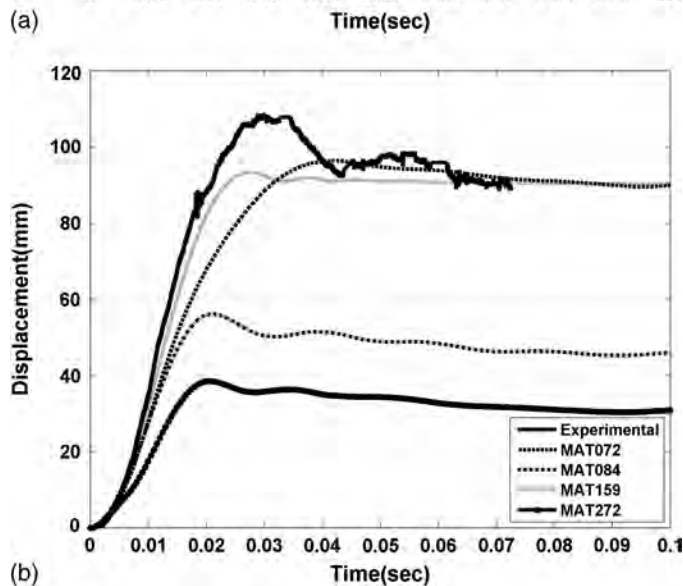
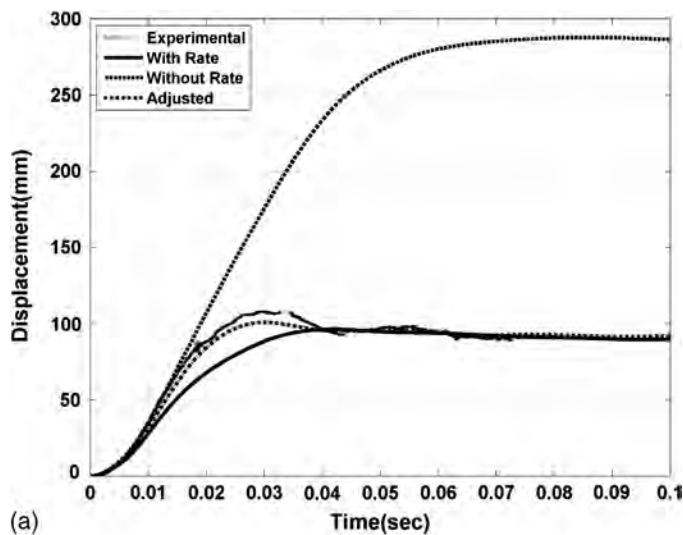


Fig. 10. Problem 3: lateral deflection histories for RC slab test: (a) by MAT072 with various conditions; (b) by various concrete models (automatic input with rate enhancement)

model demonstrates its effectiveness in calculating results when either strain rate is low or rate effects are negligible and can be ignored (Problem 2) or when strain rates are high and rate effects must be included (Problem 3). The results computed for these two problems by the KCC model aptly demonstrate the need to incorporate rate effects in a dynamic analysis.

Another observation is that the KCC model with either the default fit or the adjusted fit parameters computes roughly the same response (i.e., the value of ϖ has little impact). This is reflective of a problem in which the effects of confinement are not particularly important. However, by varying the value of ϖ , the capability afforded by a particular design with regard to its ability to gain strength and ductility, as more damage is imparted to the concrete, can be evaluated directly.

Problem 4: Scaled Aircraft Impact

In this section, a 1/7.5-scaled model test (Tsubota et al. 1999) pertaining to an aircraft impacting an RC slab was analyzed by using LS-DYNA to investigate the performance of the KCC model for impact loads. The RC slab is 1,500 mm long and 1,500 mm wide with a thickness of 60 mm. In the numerical modeling, the aircraft

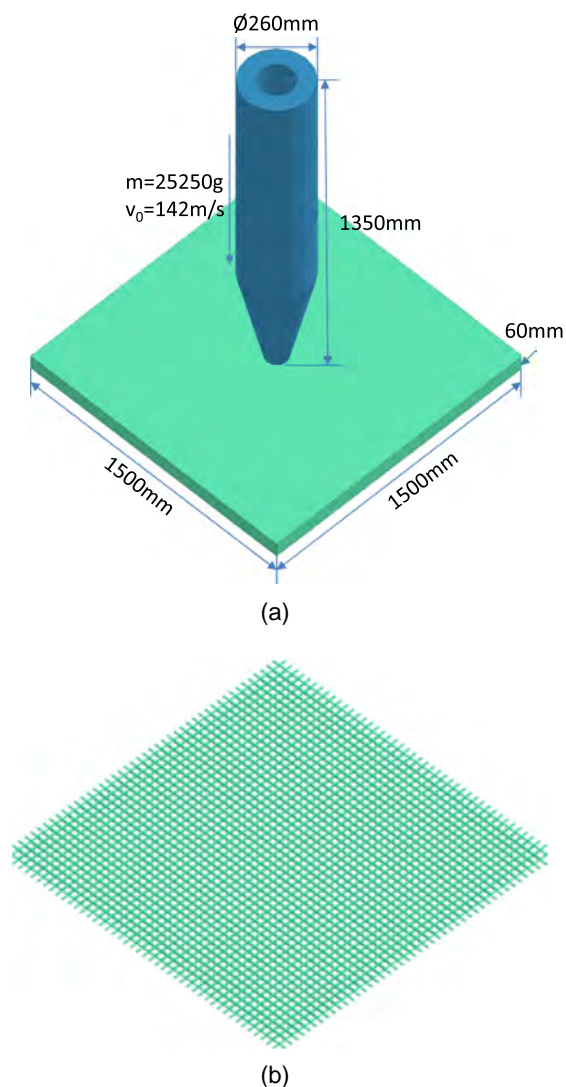


Fig. 11. Problem 4: scaled aircraft impact test: (a) simplified model; (b) distribution of D3 rebars

is idealized as a mass of 25.25 kg with an initial velocity of 142 m/s; the impact is at the center of the slab normal to its face. D3 rebars are used for the reinforcement, which are placed at 25 mm on the center each way on each face. More details about the test are described in Tsubota (1999).

The LS-DYNA model developed for this analysis is shown in Fig. 11. The concrete slab is modeled by using $12.5 \times 12.5 \times 10$ -mm (through the slab's thickness) brick elements. The concrete has an unconfined compressive strength of 31.4 MPa, which is used to scale the default fit for the strength surfaces and the EOS for the KCC model. The default damage evolution parameters are used, i.e., $b_1 = 1.60$, $b_2 = 1.35$, and $\varpi = 0.50$.

Because the analysis is performed by using a FE formulation, artificial erosion (LSTC 2014) needs to be introduced to mimic failure of the concrete; a principal strain of 20% is used for this. The rebars are modeled by beam elements sharing nodes with the concrete. The aircraft is simplified as a cylinder with a diameter of 260 mm and a length of 1,350 mm with a blunt cone head, whereas the total mass is maintained. Isotropic hardening elastoplasticity model with failure is used for both the aircraft and the rebars.

The engine velocity histories are compared in Fig. 12. The predicted exit velocity (after perforation) agrees reasonably well with the test data if MAT072 is used; the numerical prediction seems

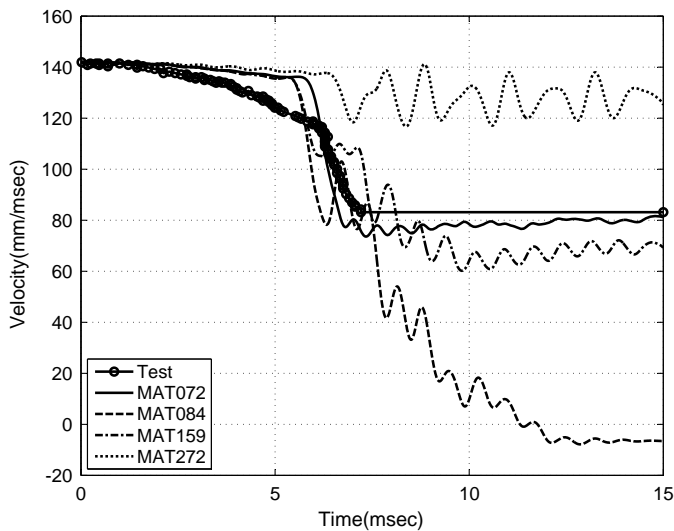


Fig. 12. Problem 4: velocity history in scaled aircraft test

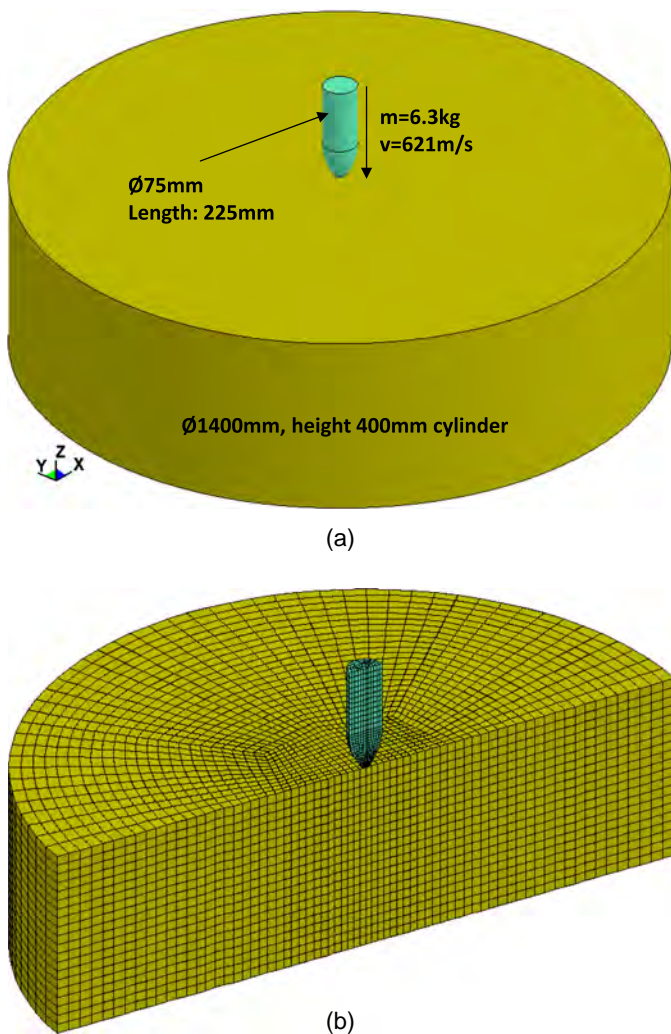
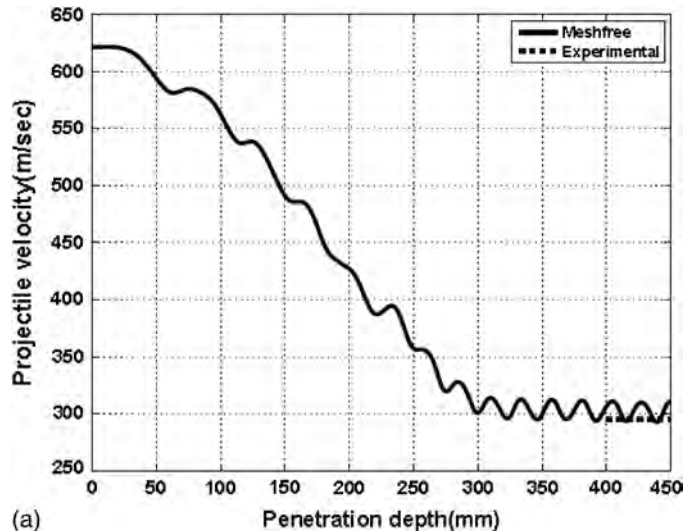
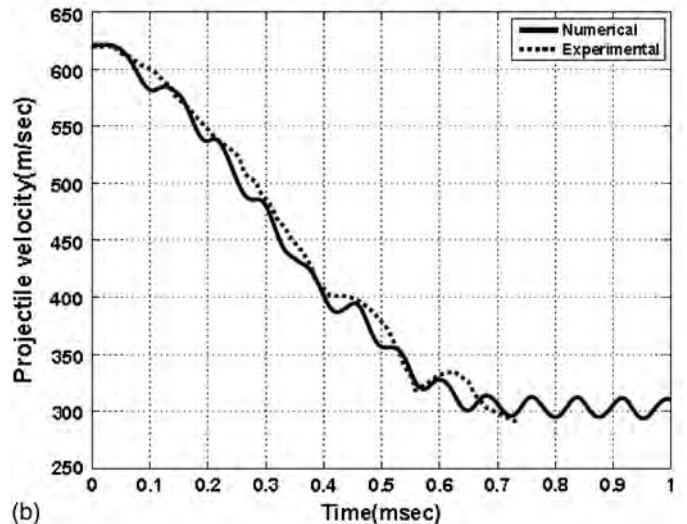


Fig. 13. Problem 5: setup of cylinder perforation test: (a) geometry; (b) discretization

acceptable if MAT159 is used; whereas the predictions with MAT084 and MAT272 are very different from the test data. It is observed that the calculated deceleration is different from the test, but the engine velocity reaches its exit value at approximately the



(a)



(b)

Fig. 14. Problem 5: projectile velocity history in cylinder perforation test: (a) velocity versus penetration depth; (b) velocity versus time

same time. However, it is arguable that a different solution might have been obtained if a different erosion criterion is introduced. This is the consequence of introducing an artificial erosion criterion. To avoid artificial erosion, the mesh-free approach is applied in solving impact problems in the next two sections.

Problem 5: Perforation Responses on High Strength Concrete

In the test carried out by Unosson and Nilsson (2006), a 6.3-kg armor-piercing steel projectile was fired at a velocity of 621 m/s at the center of the top face of a cylindrical specimen composed of a high-strength concrete. The diameter of the cylinder is 1,400 mm, and its height is 400 mm. The unconfined compressive strength of the concrete is 153 MPa, and its density is 2,770 kg/m³. The projectile has an ogival nose radius of 127 mm, a total length of 225 mm, and a diameter of 75 mm, as shown in Fig. 13.

This problem is analyzed by using KC-FEMFRE (Wu et al. 2014a), which offers an evolutionary coupling approach to analysis. By using this feature, the discretization, which initially is accomplished by using a FEM formulation, can be updated in regions with excessive mesh distortion to an RKPM formulation, which is a

mesh-free particle method that affords better accuracy and stability for regions with extreme distortions. In this way, the use of such an artificial concept as erosion to accommodate excessive distortion, which is needed with LS-DYNA, is eliminated (i.e., mesh-free methods in contrast to FE methods do not use erosion because mesh distortion is not much of an issue).

As shown in Fig. 13(b), the analysis model is initially realized by using a FEM formulation, which is discretized by 57,824 solid elements and 61,932 nodes, among which 2,144 elements and 2,439 nodes are for the projectile. The size of the elements under the impact region is approximately 13 mm.

The damage evolution parameters for the KCC model are $b_1 = 1.00$, $b_2 = 1.35$, and $\varpi = 0.50$. The projectile is modeled as elastic (Young's modulus $E = 200$ GPa and Poisson ratio $\nu = 0.33$).

The coefficient of friction between the projectile and the cylinder is 0.35.

The projectile velocity as a function of the penetration depth is shown in Fig. 14(a) along with the experimental data (Unosson and Nilsson 2006) for the projectile's residual velocity after perforation. In Fig. 14(b), both the computed and measured velocity time histories for the projectile are presented. Good correlation is observed between the numerical prediction and the test data for both penetration depth and projectile deceleration. Nearly a constant deceleration was obtained in the calculation for the projectile, which is a common observation in projectile impact tests.

The damage evolution depicted by the flight of the RKPM particles is shown in Fig. 15, in which half of the model is cut away for the sake of clarity. The legend shows the damage index ϑ , which

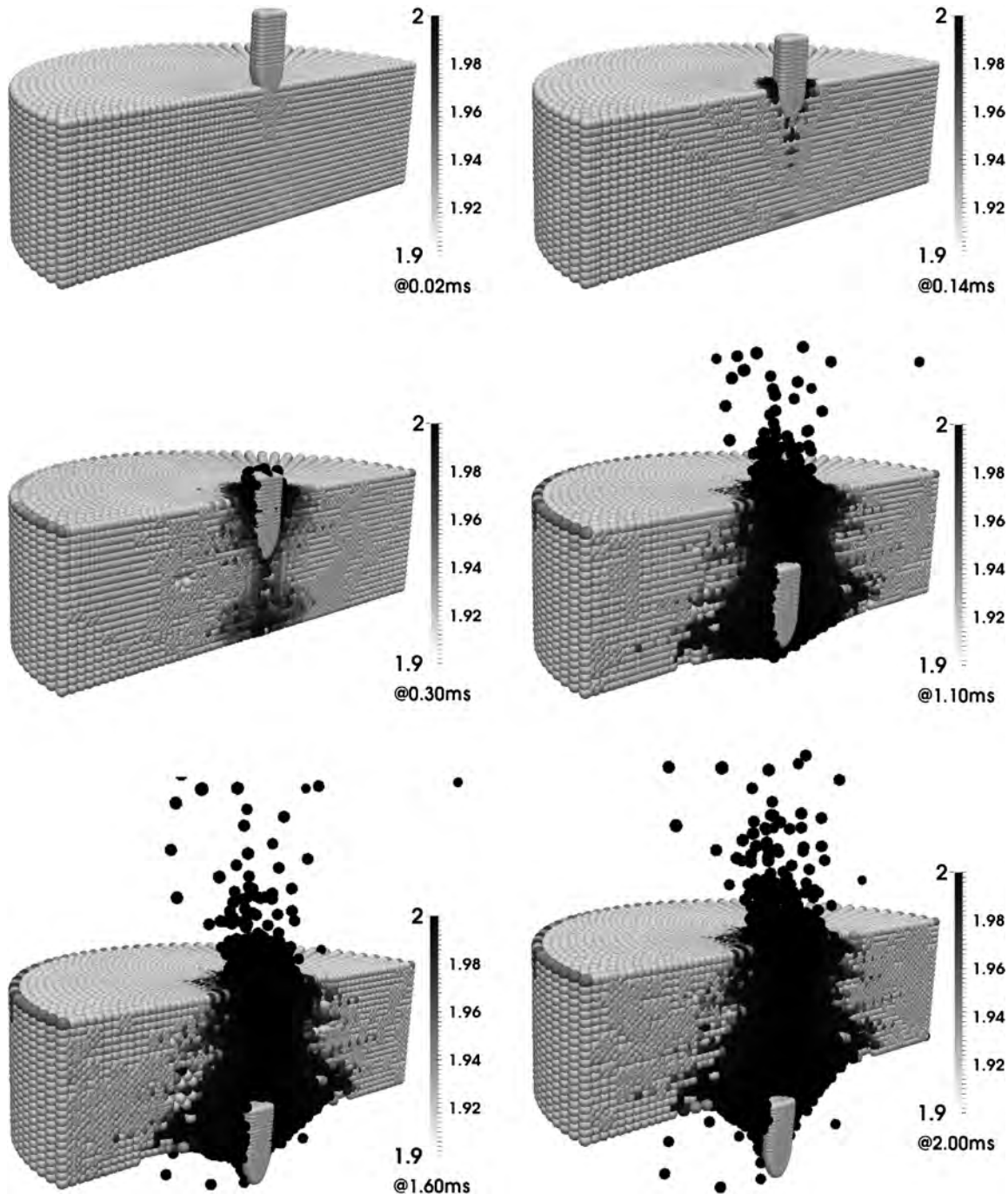


Fig. 15. Problem 5: damage evolution in cylinder perforation test

is defined in Eq. (42); $\vartheta = 1.98$ indicates that only 2% of the concrete's original strength remains, whereas $\vartheta = 1.90$ means 10% of its strength remains. As shown in the figure, the damage starts to accumulate at the top surface once the contact between the projectile and the target is initiated. Then, as the impact shock (P-wave) reaches the bottom surface and is reflected at 0.14 ms, significant damage appears at the bottom of the cylinder. When the shear wave (S-wave) reaches the edge of the cylinder at 0.3 ms, damage is observed at the edge nodes. The projectile tip is seen to penetrate through the cylinder at 1.1 ms, and finally the projectile completely perforates the cylinder at 2.0 ms. The concrete is heavily damaged along the path of the perforation.

One of the advantages provided by the nodally integrated mesh-free method (as implemented in the KC-FEMFRE) is that it tracks debris evolution naturally, which is completely unlike the artificial erosion used by finite-element methods to allow the calculation to continue when such large distortions are present. Also in marked contrast to the mesh-free characterization, which preserves the mass and momentum of the overall model, the erosion algorithm

deletes highly distorted elements (i.e., the debris) from the model, as was the case in the aircraft impact problem discussed in the fourth example.

Information characterizing the debris at the end of the perforation process is presented in Fig. 16 in terms of its mass and velocity distribution. Pieces of debris are defined as either a particle or a group of particles that have become disconnected from their neighboring particles. More than 20 thousand pieces of debris existed at the end of the perforation process. Some of the debris move as fast as 27 km/s, which could cause serious damage if it hits personnel, equipment, or conventional structural components, even though it only weighs a few grams.

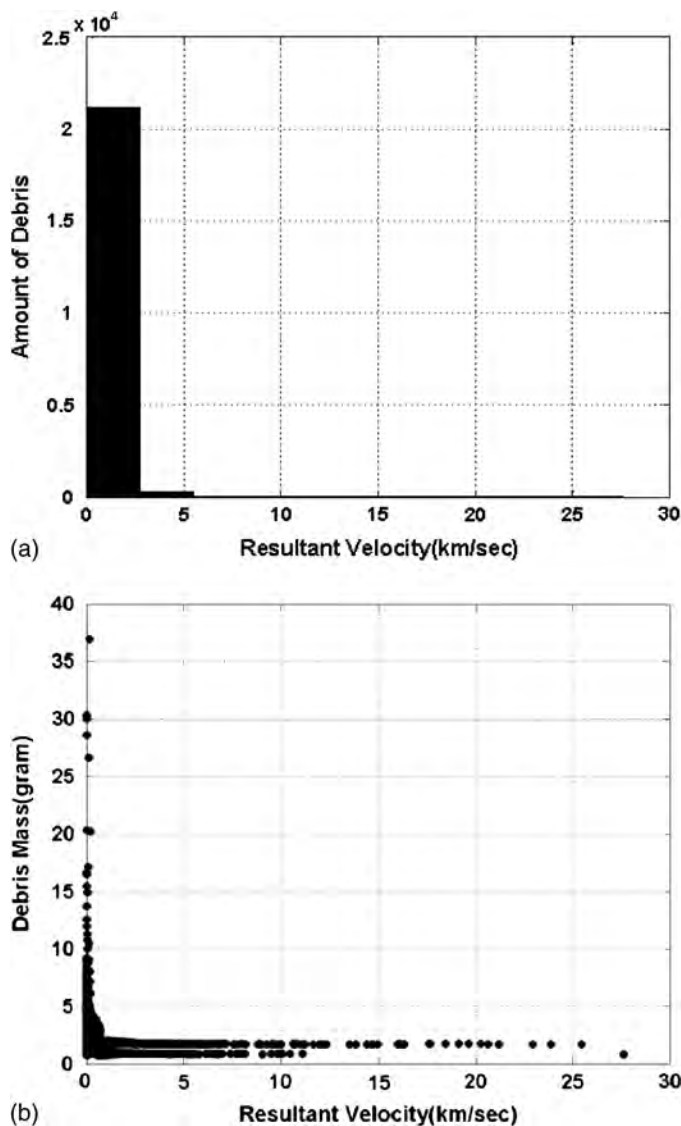


Fig. 16. Problem 5: debris distribution in cylinder perforation test: (a) amount of debris (in terms of number of particles) versus velocity; (b) mass of debris versus velocity

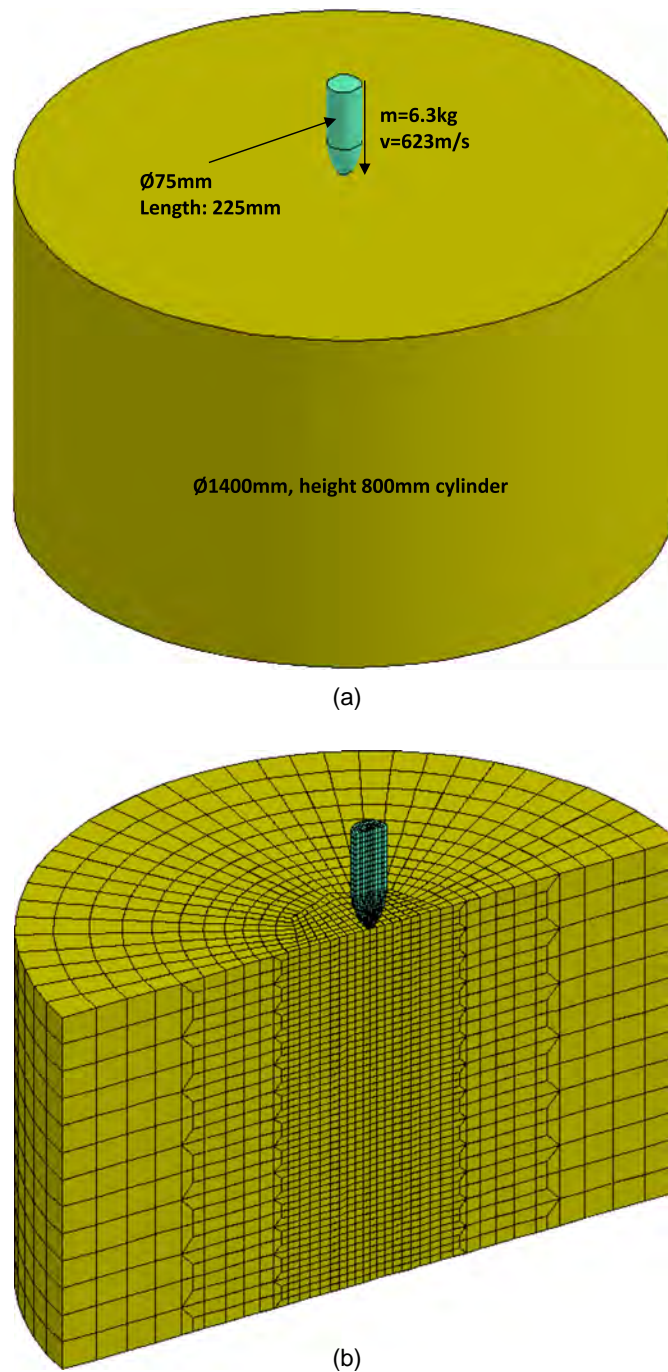


Fig. 17. Problem 6: setup of high-strength concrete penetration test: (a) geometry; (b) discretization

Problem 6: Penetration Tests for High Strength Concrete

The same projectile as used in Problem 5 was fired at a velocity of 623 m/s at the center of the face of a cylindrical specimen twice as tall as in Problem 5. This specimen is composed of the same high-strength concrete as in Problem 5, with an unconfined compressive strength of 153 MPa and density of 2,770 kg/m³. The diameter of the cylinder is 1,400 mm, and its height is 800 mm. The parameters used to characterize the materials are the same as the ones used in Problem 5 except that b_1 for the KCC model is 1.05 instead of 1.0 because large nodal distance is used.

This problem is analyzed by using KC-FEMFRE. As shown in Fig. 17, the model is initially discretized by using a FEM formulation with 36,256 solid elements and 38,044 nodes, among which 2,144 elements and 2,439 nodes are used for the projectile. To save computational cost, a variably discretizing scheme is used, as shown in Fig. 17(b), with considerably larger elements used away from the region penetrated. The size of the elements under the impact region is approximately 15 mm.

Penetration depth for the projectile as a function of time is presented in Fig. 18(a) along with the measured penetration depth

(Unosson and Nilsson 2006). The projectile velocity as a function of time is shown in Fig. 18(b). The numerical results for both penetration depth and projectile deceleration match well with test observations, again showing a relatively constant deceleration over the whole of the penetration process.

The damage evolution depicted by the flight of the RKPM particles is shown in Fig. 19. Half of the model is cut away for clarity. The legend shows the damage index ν , which is defined in Eq. (42). It can be seen that concrete damage commences at 0.02 ms. As the interaction between the projectile and the target transpires, the impact wave reaches the bottom face and is reflected at 0.3 ms. This produces damage at the bottom of the cylinder starting at approximately 1.0 ms, and spalling at the bottom face is observed. Although more and more damage is accumulated near the bottom face after 1.0 ms, the penetration peaks at approximately 1.2 ms.

As mentioned for Problem 5, the nodally integrated mesh-free method provides a natural means to track debris evolution and avoid the nonphysical and numerically questionable practices needed by the FEM discretization related to erosion and excessive mesh distortion. The debris information at the end of the penetration process is shown in Fig. 20; approximately 15 thousand pieces of debris were generated. The maximum resultant velocity of the debris is approximately 35 km/s.

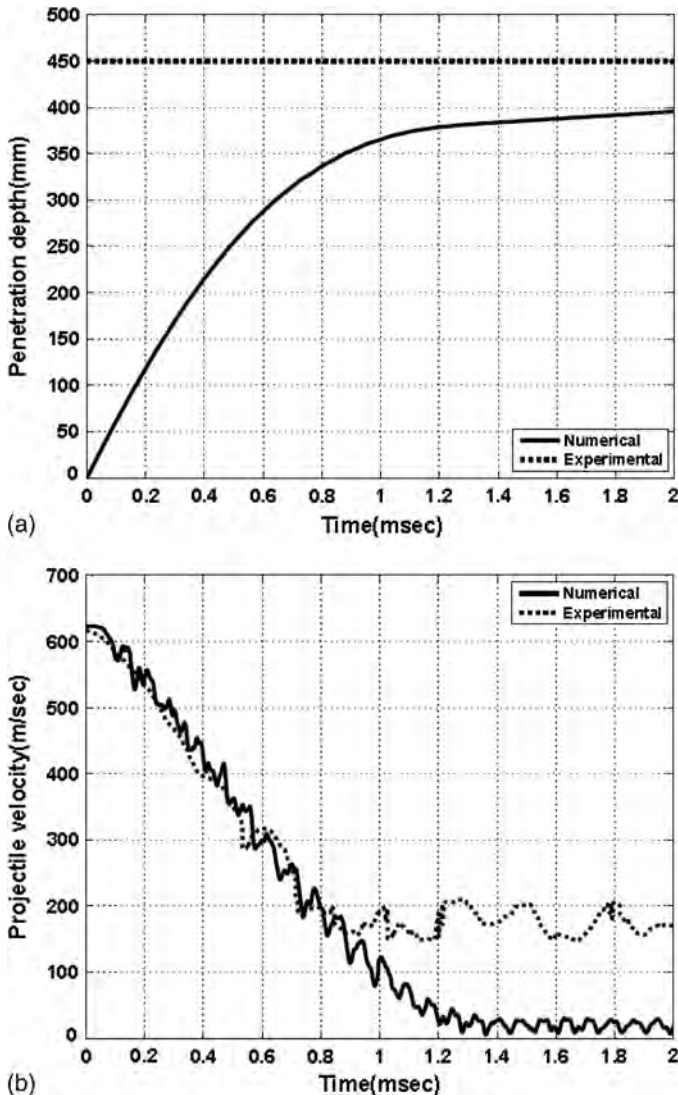


Fig. 18. Problem 6: responses in cylinder penetration test: (a) penetration depth versus time; (b) velocity versus time

Conclusions

To realistically simulate the actual responses of concrete structural components under extreme conditions (e.g., as caused by blast and impact loads) with a numerical analysis method, it is crucial to have a comprehensive, proven, and effective physics-based concrete constitutive law. The formulations, numerical implementation, parameter determination, and validation studies of such a material law—the K&C concrete model—are presented in this paper.

Modeling Studies

Modeling studies by K&C (Crawford 2013; Crawford et al. 2011, 2013) comparing the capability afforded by the different concrete models provided by LS-DYNA are quite instructive in terms of identifying the important behaviors omitted from some of these concrete models and the consequent impact on the responses such models produce when used to compute response for some sort of extreme loading of a RC structural component. These sorts of studies demonstrate the importance of evaluating firsthand the capability afforded by a particular concrete constitutive model.

Most of the extensive literature developed by K&C and others concerning the influence of parameter and model selection are omitted from this paper because of its voluminous nature, but can be found elsewhere (Crawford 2013; Crawford et al. 1997, 2011, 2012, 2013; Magallanes et al. 2010; Malvar and Crawford 1998; Malvar and Ross 1998; Malval et al. 1997; Wu et al. 2013, 2014b, c). Studies such as those conducted in the early 1990s convinced K&C that it needed to develop its own concrete model if it was to obtain results for blast effects loads that correlated well with test data.

KCC Model

The significant efforts expended by K&C over the last 20 years in formulating and calibrating concrete material models are justified because of their substantial impact on the quality of the responses computed, particularly as related to the effectiveness of the analysis in capturing realistic behaviors when extensive distress is present.

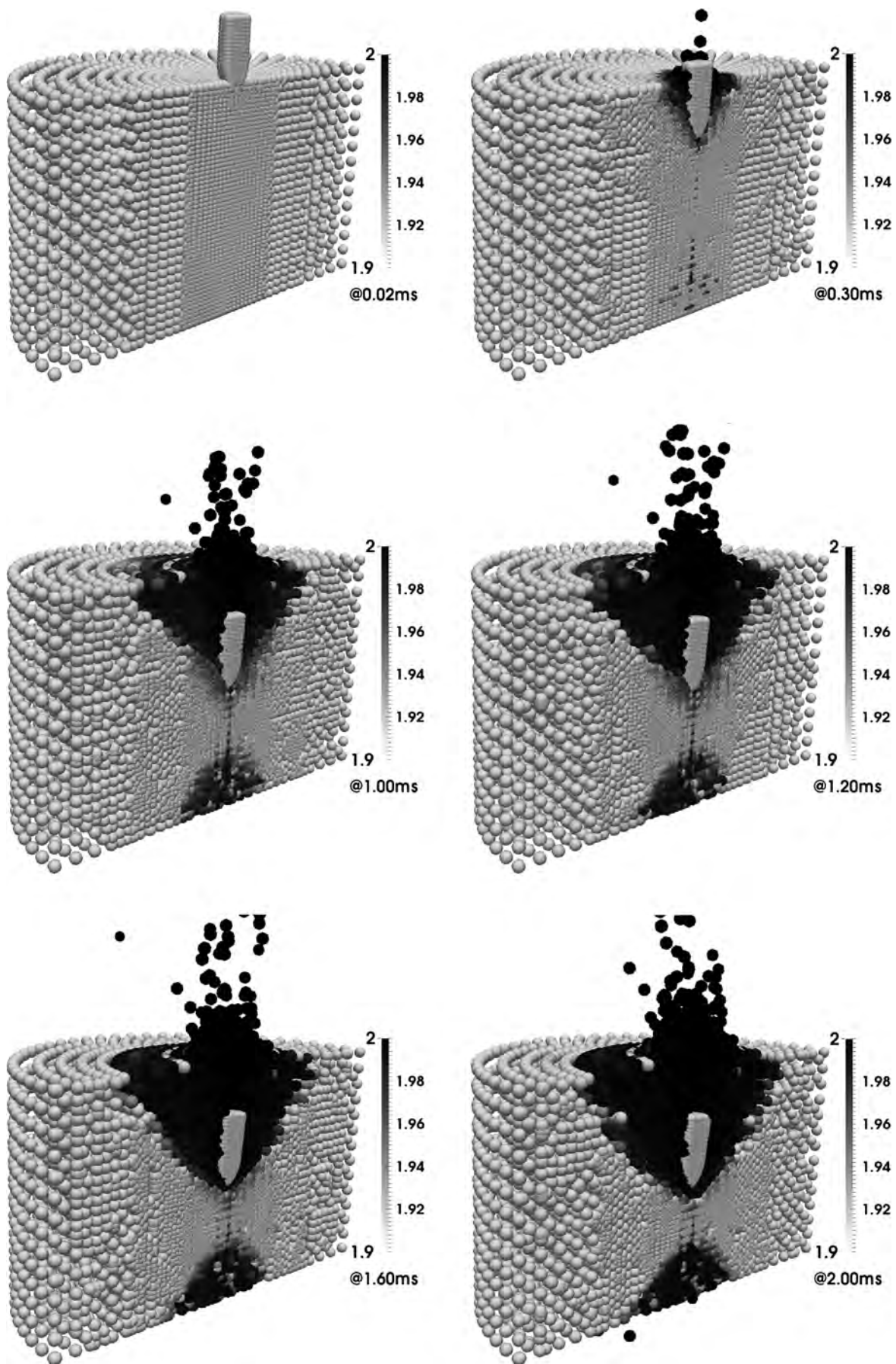


Fig. 19. Problem 6: nodal damage evolution in cylinder penetration test

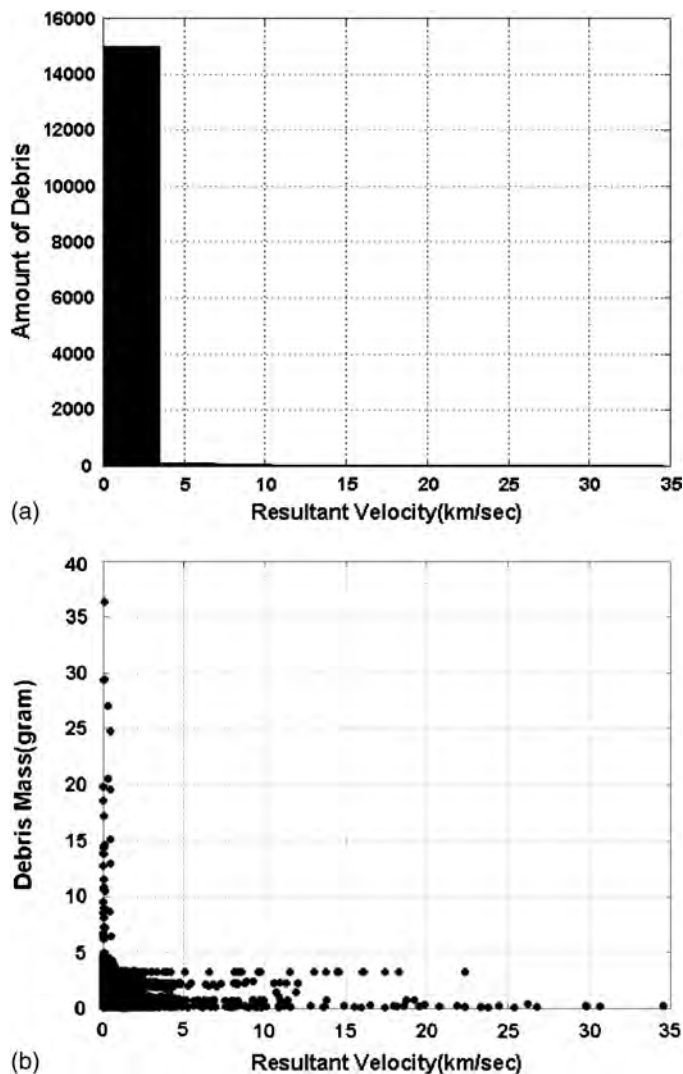


Fig. 20. Problem 6: debris distribution in cylinder penetration test: (a) distribution of velocity versus amount of debris; (b) distribution of mass versus velocity of debris

The use of physics-based material models to simulate the performance of concrete materials under blast and shock loads almost always requires that careful consideration be given to evaluating their ability to tackle the problem at hand and requires a keen knowledge of the behaviors of concrete that might be crucial to effectively predicting responses for such problems. The KCC model is a direct result of this concern for having a comprehensive and effective constitutive model to capture behaviors exhibited by cementitious materials under extreme loads.

Although the KCC model was specifically tailored to compute blast and penetration effects responses, it has proven itself applicable to a wide range of problems pertaining to the responses of concrete components, including capturing well the basic behaviors of concrete, as demonstrated in several previous papers (Crawford 2013; Crawford et al. 2011, 2012, 2013; Wu et al. 2014b) and to a limited extent in this paper (i.e., Problem 1). These basic material behaviors include the significant differences in tensile and compressive strengths, prepeak hardening (yielding), postpeak softening, transition from brittle to ductile behavior and higher strength under confinements, and strain rate effects.

The KCC model simulates the hardening and softening behaviors of concrete by using a three-surface plasticity formulation that

uses a damage function to compute a failure surface on the basis of the damage imparted to the concrete. The shape of these surfaces in the P-I plane, which is based on a Willam-Warnke formulation, allows the model to capture the difference in response between a triaxial extension and compression test. For instance, the numerical results given in this paper (Problem 1) show that the KCC model can simulate the brittle to ductile transition observed experimentally in confined triaxial tests for concrete under low to high confinement and the influence that confinement has on concrete strength.

Model Validation

Extensive model validation studies are crucial when a concrete model is intended for analyses concerning some form of extreme loading; when the prediction of failure and residual capacities are important; or when such phenomena as rate effects, confinement effects, and shear dilatancy are present. To this end, running only a few cases for a narrow class of components and load types is not a sufficient test of a material model. Although only a few results from validation studies are shown in this paper, these results do cover a wide range of problems; many more results can be found in Crawford (2013), Crawford et al. (1997, 2011, 2012, 2013) Magallanes et al. (2010; unpublished data, 2014), Malvar and Crawford (1998), Malvar and Ross (1998), Malvar et al. (1997) and Wu et al. (2013, 2014c).

A unique feature of the KCC model is its ability to model shear dilatancy. The KCC model defines the associativity level with a user input parameter ϖ . This parameter provides the flexibility needed in capturing crucial shear dilation effects related to enhancing the resistance afforded to RC columns wrapped with CFRP (Problem 2). Capturing these shear dilatancy effects accurately is particularly important in predicting the amount of CFRP wrap needed to prevent the failure of a RC column when CFRP is used to enhance its blast resistance. As shown in Problem 2, the KCC model properly captures the confinement effects exerted by CFRP wrap, which is the tensile force transferred to the CFRP as a result of the shear dilation behavior exhibited by the concrete.

The strain rate enhancement is important for concrete under high strain rate loadings such as blast and impact loads, as demonstrated by the results obtained for Problem 3. The KCC model defines this effect through a user input dynamic increase factor curve. The numerical results from the various analysis problems shown in this paper confirmed the importance of these effects and showed that the KCC model properly simulates these effects when it is activated.

The results from the validation studies for three different sorts of penetration problems are depicted in Problems 4–6. Whereas Problem 4 was solved with LS-DYNA (as were Problems 1–3), Problems 5 and 6, which involve much more severe distortions and material damage, were simulated with the KC-FEMFRE code (Wu et al. 2014a) to take advantage of the robustness afforded by its evolutionary coupling of FE and RK formulations. This coupled approach avoids using such nonphysical processes as erosion and hourglass control that often plague the performance of FE formulations. Good correlations with test data were obtained for all these problems, demonstrating the effectiveness of the KCC model in addressing penetration and perforation problems.

In summary, the robust and effective capability afforded by the KCC model was demonstrated by its ability to produce results that capture test data well, even for such complex phenomena as those pertaining to computing CFRP wrap failure (Problem 2) and projectile penetration (Problem 6). Compared with MAT084,

MAT159, and MAT272, MAT072 predicts the most consistent responses compared with test observations.

Appendix. Derivation of Increment of the Consistency Parameter $\Delta\mu$ [Eq. (32)]

To derive Eq. (32), the plastic strain increment is first defined as

$$\Delta\varepsilon_{ij}^p = \frac{\partial\varphi}{\partial\sigma_{ij}} \Delta\mu = \left(\frac{3\sigma'_{ij}}{2\sqrt{3}J_2} + \frac{\varpi\Gamma_{,p}\delta_{ij}}{3} \right) \Delta\mu \triangleq (\sigma'_{ij} + \zeta\delta_{ij})d\mu \quad (69)$$

where $\zeta = 2\varpi\Gamma_{,p}\sqrt{3}J_2/9$; and $d\mu = \frac{2}{3}\Delta\mu/\sqrt{3}J_2$.

The total strain increment can be decomposed by

$$d\boldsymbol{\varepsilon} = d\boldsymbol{\varepsilon}^p + d\boldsymbol{\varepsilon}^e = (\boldsymbol{\sigma}' + \zeta\mathbf{I})d\boldsymbol{\mu} + \mathbf{C}^{-1}:d\boldsymbol{\sigma} \quad (70)$$

where \mathbf{C} = elasticity tensor. By algebra, Eq. (70) can be converted into

$$\nabla_{\boldsymbol{\sigma}}\Upsilon:\mathbf{C}:d\boldsymbol{\varepsilon} = \nabla_{\boldsymbol{\sigma}}\Upsilon:\mathbf{C}:(\boldsymbol{\sigma}' + \zeta\mathbf{I})d\boldsymbol{\mu} + \nabla_{\boldsymbol{\sigma}}\Upsilon:d\boldsymbol{\sigma} \quad (71)$$

It follows from the definition of yield function [Eq. (2)] and $\Upsilon = 0$ after yield that

$$\nabla_{\boldsymbol{\sigma}}\Upsilon:d\boldsymbol{\sigma} = -\Upsilon_{,\lambda}d\lambda \quad (72)$$

It can be shown that $\nabla_{\boldsymbol{\sigma}}\Upsilon:\boldsymbol{\sigma}' = \sqrt{3}J_2$ and $\nabla_{\boldsymbol{\sigma}}\Upsilon:\mathbf{I} = \Gamma_{,p}$ by noticing the identities of $\mathbf{C}:\boldsymbol{\sigma}' = 2\mathbf{G}\boldsymbol{\sigma}'$ and $\mathbf{C}:\mathbf{I} = 3K\mathbf{I}$. In addition, by definition, $\mathbf{C}:d\boldsymbol{\varepsilon} = d\boldsymbol{\sigma}^*$ is the trial elastic stress increment. Therefore, Eq. (71) can be rewritten as

$$\nabla_{\boldsymbol{\sigma}}\Upsilon:d\boldsymbol{\sigma}^* = (2G\sqrt{3}J_2 + 3\zeta K\Gamma_{,p})d\mu - \Upsilon_{,\lambda}d\lambda \quad (73)$$

From Eq. (16), the increment of λ is related to the plastic strain increment by

$$\begin{aligned} d\lambda &= h(p^*)d\bar{\varepsilon}^p = h(p^*)\sqrt{\frac{2}{3}}d\varepsilon_{ij}^p d\varepsilon_{ij}^p \\ &= h(p^*)\sqrt{1 + 2\left(\frac{\varpi\Gamma_{,p}^*}{3}\right)^2} \Delta\mu \end{aligned} \quad (74)$$

Note that $\Upsilon_{,\lambda} = -\Gamma_{,\lambda}$ [from Eq. (2)]; Eq. (73) becomes

$$\nabla_{\boldsymbol{\sigma}}\Upsilon:d\boldsymbol{\sigma}^* = \left(3G + \varpi K(\Gamma_{,p}^*)^2 + \Gamma_{,\lambda}^* h(p^*) \sqrt{1 + 2\left(\frac{\varpi\Gamma_{,p}^*}{3}\right)^2} \right) \Delta\mu \quad (75)$$

Note that $\Upsilon(\boldsymbol{\sigma}^n) = 0$, and then $\Upsilon(\boldsymbol{\sigma}^*) = \Upsilon(\boldsymbol{\sigma}^n + d\boldsymbol{\sigma}^*) = \nabla_{\boldsymbol{\sigma}}\Upsilon:d\boldsymbol{\sigma}^*$. On the other hand, by definition, $\Upsilon(\boldsymbol{\sigma}^*) = \sqrt{3}J_2^* - \Gamma^*$. Therefore,

$$\Delta\mu = \frac{\sqrt{3}J_2^* - \Gamma^*}{3G + \varpi K(\Gamma_{,p}^*)^2 + \Gamma_{,\lambda}^* h(p^*) \sqrt{1 + 2\left(\frac{\varpi\Gamma_{,p}^*}{3}\right)^2}} \quad (76)$$

The quantities with a superscript * are evaluated at the trial stress, i.e., the quantities with a superscript of "trial" in Eq. (32).

References

- ACI (American Concrete Institute). (1995). "Building code requirements for reinforced concrete, and commentary." *ACI 318-95*, Farmington Hills, MI.
- ARUP. (2009). "Verification of the Karagozian and Case material model for LS-DYNA 971 R3." *124857-07*, Ove Arup & Partners, London.
- Broadhouse, B. J. (1995). "The Winfrith concrete model in LS-DYNA3D." *SPD/D (95) 363*, Safety Performance Dept., Atomic Energy Authority Technology, Winfrith, UK.
- CEB (Comite Euro-International du Beton). (1990). "CEB-FIP Model Code 90." Federation Internationale de la Precontrainte, Paris.
- Chen, J. S., Pan, C., Wu, C. T., and Liu, W. K. (1996). "Reproducing kernel particle methods for large deformation analysis of nonlinear structures." *Comput. Methods Appl. Mech. Eng.*, 139(1-4), 195-227.
- Chen, J. S., Wu, C. T., Yoon, S., and You, Y. (2001). "A stabilized conforming nodal integration for Galerkin mesh-free methods." *Int. J. Numer. Methods Eng.*, 50(2), 435-466.
- Chen, J. S., Wu, C. T., Yoon, S., and You, Y. (2002). "Nonlinear version of stabilized conforming nodal integration for Galerkin mesh-free methods." *Int. J. Numer. Methods Eng.*, 53(12), 2587-2615.
- Chen, W. F. (1982). *Plasticity in reinforced concrete*, McGraw-Hill, New York.
- Cofer, W. F., and Kohut, S. W. (1994). "A general nonlocal microplane concrete material model for dynamic finite element analysis." *Comput. Struct.*, 53(1), 189-199.
- Crawford, J. E. (2013). "State of the art for enhancing the blast resistance of reinforced concrete columns with fiber-reinforced plastic." *Can. J. Civ. Eng.*, 40(11), 1023-1033.
- Crawford, J. E., Malvar, L. J., Wesevich, J. W., Valancius, J., and Reynolds, A. D. (1997). "Retrofit of reinforced concrete structures to resist blast effects." *ACI Struct. J.*, 94(4), 371-377.
- Crawford, J. E., Wu, Y., Choi, H. J., Magallanes, J. M., and Lan, S. (2011). "User's manual and documentation for release III of the K&C concrete material model in LS-DYNA." *Technical Rep. TR-11-36.6*, Karagozian & Case, Glendale, CA.
- Crawford, J. E., Wu, Y., Magallanes, J. M., and Choi, H. J. (2013). "The importance of shear-dilatancy behaviors in RC columns." *Int. J. Prot. Struct.*, 4(3), 341-377.
- Crawford, J. E., Wu, Y., Magallanes, J. M., and Lan, S. (2012). "Modeling of concrete materials under extreme loads." *Advances in protective structures research*, H. Hao and Z.-X. Li, eds., CRC Press/Balkema, London, 1-32.
- Elsanadedy, H. M., Almusallam, T. H., Abbas, H., Al-Salloum, Y. A., and Ahsayed, S. H. (2011). "Effect of blast loading on CFRP-retrofitted RC columns—A numerical study." *Latin Am. J. Solids Struct.*, 8(1), 55-81.
- Grassl, P., Lundgren, K., and Gylltoft, K. (2002). "Concrete in compression: A plasticity theory with a novel hardening law." *Int. J. Solids Struct.*, 39(20), 5205-5223.
- Hansra, H. S. (2012). "3-D finite element modeling of reinforced concrete beam-column connections—Development and comparison to NCHRP Project 12-74." M.Sc. thesis, California State Univ., Sacramento, CA.
- Hsieh, S. S., Ting, C. E., and Chen, W. F. (1982). "A plasticity-fracture model for concrete." *Int. J. Solids Struct.*, 18(3), 181-197.
- Hu, H. T., and Schnobrich, W. C. (1989). "Constitutive modeling of concrete by using nonassociated plasticity." *J. Mater. Civ. Eng.*, 10.1061/(ASCE)0899-1561(1989)1:4(199), 199-216.
- Hughes, T. J. R., and Winget, J. M. (1980). "Finite rotation effects in numerical integration of rate constitutive equations arising in large deformation analysis." *Int. J. Numer. Methods Eng.*, 15(12), 1862-1867.
- Li, X. Q., Chen, J. F., and Lu, Y. (2011). "Meso-scale modeling of FRP-to-concrete bond behavior using LS-DYNA." *Advances in FRP Composites in Civil Engineering*, Springer, Berlin, 494-498.
- Lin, J. I. (2005). "DYNA3D: A nonlinear, explicit, three-dimensional finite element code for solid and structural mechanics, user manual." *UCRL-MA-107254*, Lawrence Livermore National Laboratory, Livermore, CA.
- Lin, X., Zhang, Y. X., and Hazell, P. J. (2013). "Modelling the response of reinforced concrete panels under blast loading." *Mater. Des.*, 56, 620-628.

- Liu, W. K., Jun, S., and Zhang, Y. F. (1995). "Reproducing kernel particle methods." *Int. J. Numer. Methods Fluids*, 20(8–9), 1081–1106.
- Löhner, R., et al. (2002). "Advances in FEFLO." *AIAA-02-1024*, School of Computational Sciences, George Mason Univ., Fairfax, VA.
- LSTC (Livermore Software Technology Corporation). (2014). *LS-DYNA keyword user's manual, Vol. 1*, Livermore, CA.
- Magallanes, J. M., Wu, Y., Malvar, L. J., and Crawford, J. E. (2010). "Recent improvements to release III of the K&C concrete model." *Proc., 11th Int. LS-DYNA® Users Conf.*, LSTC, Livermore, CA.
- Malvar, L. J., and Crawford, J. E. (1998). "Dynamic increase factors for concrete." *Proc., 28th DDES Seminar*, DDES, Alexandria, VA.
- Malvar, L. J., Crawford, J. E., Wesevich, J. W., and Simons, D. (1997). "A plasticity concrete material model for DYNA3D." *Int. J. Impact Eng.*, 19(9–10), 847–873.
- Malvar, L. J., and Ross, C. A. (1998). "Review of strain rate effects for concrete in tension." *ACI Mater. J.*, 95(6), 735–739.
- Meschke, G., Lackner, R., and Mang, H. A. (1998). "An anisotropic elastoplastic-damage model for plain concrete." *Int. J. Numer. Methods Eng.*, 42(4), 703–727.
- Morrill, K. B., Malvar, L. J., and Crawford, J. E. (1998). "PRONTO3D user's manual for modeling reinforced concrete." *Technical Rep.*, Karagozian & Case, Burbank, CA.
- Mroz, Z. (1967). "On the description of anisotropic workhardening." *J. Mech. Phys. Solids*, 15(3), 163–175.
- Mroz, Z., Norris, V. A., and Zienkiewicz, O. C. (1978). "An anisotropic hardening model for soils and its application to cyclic loading." *Int. J. Numer. Anal. Methods Geomech.*, 2(3), 203–221.
- Murray, Y. D. (2007). "Users manual for LS-DYNA concrete material model 159." *Rep. No. FHWA-HRT-05-062*, Federal Highway Administration, Washington, DC.
- Ottosen, N. S. (1977). "A failure criterion for concrete." *J. Eng. Mech.*, 103(4), 527–535.
- Papa, E., and Taliercio, A. (1996). "Anisotropic damage model for the multiaxial static and fatigue behavior of plain concrete." *Eng. Fract. Mech.*, 55(2), 163–179.
- Rabczuk, T., and Eibl, J. (2003). "Simulation of high velocity concrete fragmentation using SPH/MLSPH." *Int. J. Numer. Methods Eng.*, 56(10), 1421–1444.
- Riedel, W., Thomas, K., Hiermaier, S., and Schmolinske, E. (1999). "Penetration of reinforced concrete by BETA-B-500 numerical analysis using a new macroscopic concrete model for hydrocodes." *Proc., 9th Int. Symp. on Interaction of the Effects of Munitions with Structures*, Berlin, 315–322.
- Schwer, L. E., and Murray, Y. D. (1994). "A three-invariant smooth cap model with mixed hardening." *Int. J. Numer. Anal. Methods Geomech.*, 18(10), 657–688.
- Simo, J. C., and Hughes, T. J. R. (1998). *Computational inelasticity*, Springer, New York.
- Tsubota, H., et al. (1999). "Scale model tests of multiple barriers against aircraft impact: Part 1. Experimental program and test results." *Proc., Transactions of the 15th Int. Conf. on Structural Mechanics in Reactor Technology (SMiRT-15)*, Seoul.
- Unosson, M., and Nilsson, L. (2006). "Projectile penetration and perforation of high performance concrete: Experimental results and macroscopic modeling." *Int. J. Impact Eng.*, 32(7), 1068–1085.
- Willam, K. J., and Warnke, E. P. (1975). "Constitutive model for the triaxial behavior of concrete." *Proc., Int. Association for Bridge and Structural Engineering*, ISMES, Bergamo, Italy, 174–186.
- Wu, Y., Choi, H. J., and Crawford, J. E. (2014a). "KC-FEMFRE user's manual (Karagozian & Case finite element and mesh-free analysis program)." *Technical Rep. TR-14-2*, Karagozian & Case, Glendale, CA.
- Wu, Y., Crawford, J. E., Lan, S., and Magallanes, J. M. (2014b). "Validation studies for concrete constitutive models with blast test data." *Proc., 13th Int. LS-DYNA® Users Conf.*, LSTC, Livermore, CA.
- Wu, Y., Magallanes, J. M., Choi, H. J., and Crawford, J. E. (2013). "An evolutionarily coupled finite-element mesh-free formulation for modeling concrete behaviors under blast and impact loadings." *J. Eng. Mech.*, 10.1061/(ASCE)EM.1943-7889.0000497, 525–536.
- Wu, Y., Magallanes, J. M., and Crawford, J. E. (2014c). "Fragmentation and debris evolution modeled by a point-wise coupled reproducing kernel—Finite element formulation." *Int. J. Damage Mech.*, 23(7), 1005–1034.
- Yazdani, S., and Schreyer, H. L. (1988). "An anisotropic damage model with dilation for concrete." *Mech. Mater.*, 7(3), 231–244.